Intraseasonal Variation of Winter Precipitation over the Western United States Simulated by 14 IPCC AR4 Coupled GCMs

Jia-Lin Lin[1], Taotao Qian[1,2], Toshiaki Shinoda[3], Weiqing Han[4], Paul Roundy[5], and Yangxing Zheng[6]

[1]Department of Geography, The Ohio State University, Columbus, OH
[2]Byrd Polar Research Center, The Ohio State University, Columbus, OH
[3]Naval Research Laboratory, Stennis Space Center, MS
[4]Department of Atmospheric and Oceanic Sciences, University of Colorado, Boulder, CO
[5]State University of New York, Albany, NY
[6]NOAA ESRL/CIRES Climate Diagnostics Center, Boulder, CO

J. Climate
Submitted August 2008; Revised November 2008

Corresponding author address: Dr. Jia-Lin Lin
Department of Geography, The Ohio State University
1105 Derby Hall, 154 North Oval Mall, Columbus, OH 43210
Email: lin.789@osu.edu

Abstract

This study evaluates the intraseasonal variation of winter precipitation over the western United States in 14 coupled general circulation models (GCMs) participating in the Inter-governmental Panel on Climate Change (IPCC) Fourth Assessment Report (AR4). Eight years of each model's 20th century climate simulation are analyzed. We focus on the two dominant intraseasonal modes for the western U.S. precipitation: the 40-day mode and the 22-day mode.

The results show that the models tend to overestimate the northern winter (November to April) seasonal mean precipitation over the western United States and Canada. The models also tend to produce overly strong intraseasonal variability in western U.S. wintertime precipitation, in spite of the overly weak tropical intraseasonal variability in most of the models. All models capture both the 40-day mode and the 22-day mode, usually with overly large variances. For the 40-day mode, models tend to reproduce its deep barotropic vertical structure and three-cell horizontal structure, but only five of the 14 models capture its northward propagation, and only two models simulate its teleconnection with the Madden-Julian Oscillation in tropical Pacific. For the 22-day mode, eight of the 14 models reproduce its coherent northward propagation, and nine models capture its teleconnection with precipitation in tropical Pacific.

1. Introduction

The western United States normally receives the bulk of its precipitation during Northern Hemisphere (NH) winter from October to April when the storm track across the North Pacific is active, and the precipitation is characterized by distinct wet and dry episodes at the intraseasonal time-scale (Mo and Higgins 1998a, 1998b, Mo 1999). As demonstrated by Mo (1999), the intraseasonal variability of western U.S. winter precipitation has two dominant modes: a mode with a period of about 36-40 days (hereafter the 40-day mode) and a mode with a period of about 20-25 days (hereafter the 22-day mode). Previous studies have found three mechanisms for generating the intraseasonal variability of western U.S. winter precipitation (Figure 1): (1) instability of the basic state (e.g. Simmons et al. 1983; Schubert 1986; Frederiksen 1986; Dole and Black 1990; Schubert et al. 1993), (2) orographic forcing (Marcus et al. 1994, 1996), (3) interactions with synoptic-scale eddies (Lau 1988; Held et al. 1989), and (4) forcing of tropical convection (Mo and Higgins 1998a, 1998b, Mo 1999). Of particular importance for extended-range weather forecasts is the tropical forcing mechanism. As shown by Mo (1999), the 40-day mode is related to the Madden-Julian Oscillation (MJO) in the tropics with enhanced convection propagating from the western Pacific to the central Pacific and exciting a three-cell pattern, leading to enhanced precipitation in California. When enhanced convection moves to the central Pacific, the response in the Northern Hemisphere resembles the Pacific–North American teleconnection pattern (PNA; Wallace and Gutzler 1981; Weickmann et al. 1985). The 22-day mode is also related to tropical convection with cloud bands propagating northward along the west coast of North America from the eastern Pacific through California to the Pacific Northwest.

These intraseasonal modes are responsible for alternating wet and dry episodes over the western United States. However, only a few previous studies have examined their simulations by the general circulation models (GCMs). In a pioneering study, Schubert et al. (1993) examined the simulations by an atmospheric GCM developed at the NASA Goddard Laboratory for Atmospheres. They found that the GCM's leading mode in the upper-tropospheric zonal wind is associated with fluctuations of the East Asian jet; this mode resembles the structure of the PNA pattern found in the observations on these time scales. The GCM produces 60% of the total observed Pacific sector low-frequency zonal wind variance. About one-third of the missing variability appears to be due to unrealistic simulations of the MJO.

Recently, in preparation for the Inter-governmental Panel on Climate Change (IPCC) Fourth Assessment Report (AR4), more than a dozen international climate modeling centers conducted a comprehensive set of long-term simulations for both the 20th century's climate and different climate change scenarios in the 21st century (Randall et al. 2007). Before conducting the extended simulations, many of the modeling centers applied an overhaul to their physical schemes to incorporate the state-of-the-art research results. For example, almost all modeling centers have implemented prognostic cloud microphysics schemes to their models, some have added a moisture trigger to their deep convection schemes, and some now take into account convective momentum transport. Moreover, many modeling centers increased their models' horizontal and vertical resolutions and some conducted experiments with different resolutions.

The purpose of this study is to evaluate the intraseasonal variation of precipitation over the western United States in 14 IPCC AR4 coupled GCMs, with emphasis on the 40-

day mode and the 22-day mode. The models and validation datasets used in this study are described in section 2. The diagnostic methods are described in section 3. Results are presented in section 4. A summary and discussion are given in section 5.

2. Models and validation datasets

This analysis is based on eight years of the Climate of the 20th Century (20C3M) simulations from 14 coupled GCMs. Table 1 shows the model names and acronyms, their horizontal and vertical resolutions, and brief descriptions of their deep convection schemes. For each model we used eight years of daily mean surface precipitation. Three-dimensional data are available for seven of the 14 models, for which we analyzed upper air winds, temperature and specific humidity.

The model simulations were validated using the Global Precipitation Climatology Project (GPCP) Version 2 Precipitation (Huffman et al. 2001). We used eight years (1997-2004) of daily data with a horizontal resolution of 1 degree longitude by 1 degree latitude. Obtaining reliable precipitation estimates, especially over the open ocean area where surface observations are sparse, continues to be a big challenge for the research community and was the motivation for the international GPCP project. The GPCP dataset is a merged analysis incorporating available precipitation estimates from low-orbit-satellite microwave data, geosynchronous-orbit-satellite infrared data, and rain gauge observations. Gruber and Levizzani (2008) provided a detailed assessment of the GPCP dataset. The data quality varies significantly from region to region. Fortunately, the region of interest for this study (the western United States and surrounding areas) is

associated with relatively good data quality although substantial uncertainties still exist (see Fig. 2.2 of Gruber and Levizzani 2008).

To evaluate the model-simulated atmospheric circulation, we also used eight years (1997-2004) of daily National Center for Environmental Prediction (NCEP) reanalysis data (Kalnay et al. 1996), for which we analyzed upper air winds, temperature and specific humidity. There are possible errors associated with the reanalysis data coming from measurement errors, poor data coverage over certain geographical regions and effects of assimilation models. However, previous studies have shown that the errors could be significantly reduced by spatial averaging over many grid points and constructing composite over many events (e.g. Carr and Bretherton 2001; Lin et al. 2005, 2008).

3. Methods

Total intraseasonal (periods 10-90 days) anomalies were obtained by applying a 365-point 10-90 day Lanczos filter (Duchan 1979). Because the Lanczos filter is non-recursive, 182 days of data were lost at each end of the time series (364 days in total). The dominant intraseasonal modes are determined using wavelet spectrum because they are active mainly during the southern summer. Wavelet spectrum is a powerful tool for analyzing multi-scale, nonstationary processes, and can simultaneously determine both the dominant modes of variability and how those modes vary in time (e.g. Mak 1995; Torrence and Compo 1997). We utilize the wavelet analysis program developed by Torrence and Compo (1997) and use the Morlet wavelet as the mother wavelet. We have tested different mother wavelets (Paul or Derivative of Gaussian) and the results are

similar. The 40-day mode is defined as precipitation variability in the period range of 30-60 days, and was obtained by applying a 365-point 30-60 day Lanczos filter. Similarly, the 22-day mode is defined as precipitation variability in the period range of 20-30 days, and was obtained by applying a 365-point 20-30 day Lanczos filter. We also tested the Murakami (1976) filter and the results are similar.

4. Results

a Northern winter (November-April) seasonal mean precipitation

Previous observational studies indicate that the intraseasonal variance of precipitation is highly correlated with time-mean precipitation (e.g. Wheeler and Kiladis 1999). Therefore we first look at the horizontal distribution of Northern winter (November-April) seasonal mean precipitation (Figure 2). If we use the 2 mm/day contour to define the gross horizontal pattern of precipitation in observation, all 14 models capture reasonably this gross pattern. In particular, they all produce the NE-SW tilted north Pacific storm track. Most of them also reproduce the peak along the west coast of the United States and Canada. The eastern Pacific ITCZ is also reasonably simulated by all models although with a large variation in precipitation magnitude.

To conduct a more quantitative evaluation of the seasonal mean precipitation over the western United States, we plot in Figure 3 the meridional profile averaged between 235E-245E. There is a wide spread among the models. All but two models (MRI and GISS-ER) overestimate the precipitation by more than 30%. The MRI model precipitation is in excellent agreement with observation. The precipitation peak is shifted slightly northward

in one model (GISS-ER) but slightly southward in two other models (GISS-AOM and IPSL).

b Total intraseasonal (10-90 day) variance

Figure 4 shows the horizontal distribution of the total intraseasonal (10-90 day) variance of precipitation during northern winter (November-April). In observation (Figure 4a), the horizontal distribution of total intraseasonal variance follows that of seasonal mean precipitation (Figure 2), except that the variance over north Pacific storm track is shifted slightly southward comparing to the seasonal mean precipitation. The model variances show three characteristics. First, all models capture the basic spatial pattern of the variance including the slight southward shift comparing to the seasonal mean precipitation. Second, most models produce overly large variance along the west coast of the United States and Canada. Third, all models underestimate the variance over the north Pacific Ocean, in spite of the fact that they generally produce reasonable seasonal mean precipitation in that region (Figure 2). This suggests an interesting land-sea contrast in the models ability to simulate extratropical intraseasonal variability with a better performance over land than over ocean.

To provide a more quantitative evaluation of the model simulations, Figure 5 shows the meridional profile of total intraseasonal (10-90 day) variance of precipitation averaged between 235E-245E. Over the western United States and Canada, all but two models (MRI and GISS-ER) produce a variance that is 2-7 times of the observed variance, which is consistent with their overly large seasonal mean precipitation (Figure 3). This is in sharp contrast with the models simulations of tropical intraseasonal

variability (Lin et al. 2006). Although the models generally produce reasonable seasonal mean tropical precipitation, only a few of them could simulate reasonable tropical intraseasonal variability, suggesting that the tropical intraseasonal variability is generated by mechanisms different from the extratropical intraseasonal variability.

c The dominant intraseasonal modes

Figure 6 shows the wavelet spectrum of precipitation averaged between 40-45N and 235-245E for observation and the 14 IPCC models. The Morlet wavelet was used as the mother wavelet. We have tested different mother wavelets (Paul or Derivative of Gaussian) and the results look similar. The observed spectrum (Figure 6) demonstrates two dominant intraseasonal modes, a 30-60 day mode (the so-called 40-day mode) and a 15-30 day mode (the so-called 22-day mode). All models capture both modes, and the model variances are generally larger than the observed variances. The models also tend to produce more frequent active episodes.

d The 40-day mode

Next we focus on the 40-day mode. Figure 7 shows the meridional profile of the 40-day mode variance averaged between 235E-245E. For both the observation and the models, the spatial distribution of the 40-day mode variance looks quite similar to that of the total intraseasonal variance. All but one model (MRI) produce 2-9 times of observed 40-day mode variance over the western United States and Canada. The MRI model variance is in very good agreement with the observed variance.

Figure 8 shows the lag-correlation of the 40-day mode precipitation anomaly averaged between 235E-245E with respect to itself at 37.5N240E. Shading denotes the regions where lag-correlation is above the 95% confidence level. In observation (Figure

8a), the 40-day mode propagates northward from 10N to 50N, which is consistent with the results of Mo (1999). Five of the 14 models simulate coherent northward propagations (GFDL2.0, CCSM3, MRI, CGCM, IPSL). Two models produce standing oscillation (GFDL2.1, PCM), while the other seven models simulate southward propagations (GISS-AOM, GISS-ER, MIROC-medres, MIROC-hires, MPI, CNRM, and CSIRO).

Next we look at the vertical structures of the 40-day mode. Figure 9 shows the vertical structure of temperature for observation (NCEP reanalysis) and seven models with three-dimensional data available. Note that for four models the 3-D data is available only below 200 mb. In observation, the 40-day mode displays a two-layer structure during the precipitating phase, with a cold core between surface and 250 mb, and a warm core above 250 mb. Five of the seven models (GFDL2.0, GFDL2.1, CGCM, MPI and CNRM) reproduce the two-layer structure. In GISS-AOM the two-layer structure is shifted to the later phase by about 7 days. MRI simulates a cold core between 200 mb and 850 mb, and a warm core below 850 mb.

Figure 10 shows the vertical structure of geopotential height. Consistent with the temperature structure, the observed geopotential height displays a deep barotropic structure, with negative anomaly extending from the surface to 100 mb during the precipitating phase (Figure 10a). All models reproduce the deep barotropic structure. However, in four models the correlation is low in the upper troposphere (GFDL2.1, GISS-AOM, MRI and MPI).

Figure 11 shows the vertical structure of divergence. The observed divergence displays a two-layer structure during the precipitating phase, with convergence from the

surface to 650 mb, and divergence above 650 mb (Figure 11a). All but one model (MPI) reproduce fairly well the two-layer structure, although in GISS-AOM (Figure 11d) the convergence layer is too deep, extending from the surface to 450 mb.

Next we look at the teleconnection pattern associated with the 40-day mode. Figure 12 shows the linear correlation of the 40-day mode precipitation anomaly versus itself averaged between 35N-40N, 235E-245E. In observation (Figure 12a), there is a three-cell pattern with positive precipitation anomaly over the western United States and negative anomalies over the eastern Pacific and the Pacific Northwest. At the same time, there is a dipole over tropical Pacific with positive anomaly in central Pacific and negative anomaly in western Pacific. These are consistent with the results of Mo (1999; her Figure 5c), and Mo demonstrated that the dipole over tropical Pacific is associated with the MJO. Most of the models simulate to some extent the three-cell pattern around the western United States. However, only two models (CCSM3 and PCM) simulate the dipole over tropical Pacific. Four other models (GISS-AOM, GISS-ER, MIROC-medres, MIROC-hires) produce statistically significant positive anomaly in central Pacific, but no statistically significant negative anomaly in western Pacific.

To summarize, the models tend to simulate overly large variance of the 40-day mode over the western United States and Canada. All models with three-dimensional data available reproduce the deep barotropic structure of the 40-day mode. All models reproduce to some extent the three-cell pattern of precipitation anomaly around the western United States, but only five models capture the northward propagation and only two models simulate the teleconnection with the MJO in tropical Pacific.

e The 22-day mode

Figure 13 shows the meridional profile of the 22-day mode variance averaged between 235E-245E. For both the observation and the models, the spatial distribution of the 22-day mode variance looks quite similar to that of the total intraseasonal variance and the 40-day mode. Eleven of the 14 models (GFDL2.0, GFDL2.1, CCSM3, PCM, GISS-AOM, MIROC-medres, MIROC-hires, CCGCM, MPI, IPSL, and CSIRO) produce more than 2 times of observed 22-day mode variance over the western United States and Canada, while three models (MRI, CNRM, and GISS-ER) produce variances that are very close to the observed value.

Figure 14 shows the lag-correlation of the 22-day mode precipitation anomaly averaged between 235E-245E with respect to itself at 37.5N240E. In observation (Figure 14a), the 22-day mode propagates northward from the equator to 45N, which is consistent with the results of Mo (1999). Nine of the 14 models simulate coherent northward propagation (GFDL2.0, GFDL2.1, CCSM3, GISS-ER, MIROC-hires, MRI, CGCM, MPI, CSIRO). Two models produce standing oscillation (GFDL2.1, GISS-AOM, CNRM), one model simulates southward propagation (PCM), and two models display different propagation direction in different regions (MIROC-medres, IPSL).

Figure 15 shows the teleconnection pattern of the 22-day mode. In observation (Figure 15a), there is a positive anomaly extending from western United States to 15N210E, a positive anomaly around 15S210E, and a negative anomaly around 15N130E. Nine of the 14 models reproduce statistically significant positive anomaly around 15N210E (GFDL2.0, CCSM3, GISS-AOM, GISS-ER, MIROC-medres, MIROC-hires, IPSL, CNRM, CSIRO), although in some models it is shifted slightly northward

(e.g. GFDL2.0, CCSM3). Three models reproduce statistically significant positive anomaly around 15S210E (MIROC-hires, CSIRO and GFDL2.1), and only one model simulates statistically significant negative anomaly around 15N130E (CSIRO).

5. Summary and discussion

This study evaluates the intraseasonal variation of winter precipitation over the western United States in 14 IPCC AR4 coupled GCMs. The results show that the models tend to overestimate the northern winter (November to April) seasonal mean precipitation over the western United States and Canada. The models also tend to produce overly strong intraseasonal variability in western U.S. wintertime precipitation, in spite of the overly weak tropical intraseasonal variability in most of the models. All models capture both the 40-day mode and the 22-day mode, usually with overly large variances. For the 40-day mode, models tend to reproduce its deep barotropic vertical structure and three-cell horizontal structure, but only five of the 14 models capture its northward propagation, and only two models simulate its teleconnection with the Madden-Julian Oscillation in tropical Pacific. For the 22-day mode, eight of the 14 models reproduce its coherent northward propagation, and nine models capture its teleconnection with precipitation in tropical Pacific.

The above results have two implications on the dynamics of intraseasonal variability of western U.S. winter precipitation. First, in spite of the lack of MJO and overly weak tropical intraseasonal variability in most of the models, they still produce overly strong intraseasonal variability of western U.S. winter precipitation, suggesting that tropical forcing may be a secondary mechanism for generating this variability. This is consistent

with several previous studies (e.g. Lau 1981; Simmons et al. 1983; Karoly et al. 1989; Schubert and Park 1991; Schubert et al. 1993).

Secondly, a new finding of this study is that several models could reproduce the northward propagation of the 40-day mode with the lack of MJO signals in those models. This suggests that the northward propagation of the 40-day mode may not be generated by the Rossby wave emanation from the tropical MJO. Theoretical and observational studies have suggested several different mechanisms for northward propagation of intraseasonal modes, including land surface heat flux (Webster 1983; Srinivasan et al. 1993), ocean surface sensible heat flux (Hsu et al. 2004), vertical-shear-induced boundary layer moisture convergence (Jiang et al. 2004), and moisture advection (Jiang et al. 2004). In future studies, analyses of heat, moisture and vorticity budgets are needed to examine if these mechanisms contribute to the northward propagations in the models.

Among the 14 coupled GCMs, the MRI model arguably produces the best overall intraseasonal variability of western U.S. precipitation. As shown in Table 1, the resolution of the MRI model lies in the middle among the 14 models. The MRI model also has quite similar model physics as the other two Japanese models (MIROC-hires and MIROC-medres), but produces different intraseasonal variability. Because of the complicated mechanisms for generating the intraseasonal variability as discussed above, further analyses are needed to understand the better performance of the MRI model.

One major caveat of this study is the substantial uncertainties associated with the precipitation observations, which have been discussed briefly in section 2. Currently, NASA is planning its Global Precipitation Measurement (GPM) Mission to improve our measurements of precipitation over both the tropics and extratropics. We expect that the

next generation of precipitation analysis will provide a more solid benchmark for evaluating the climate model simulations.

Acknowledgements

Gary Russell kindly provided detailed description of the GISS-AOM model. We acknowledge the international modeling groups for providing their data for analysis, the Program for Climate Model Diagnosis and Intercomparison (PCMDI) for collecting and archiving the model data, the JSC/CLIVAR Working Group on Coupled Modeling (WGCM) and their Coupled Model Intercomparison Project (CMIP) and Climate Simulation Panel for organizing the model data analysis activity, and the IPCC WG1 TSU for technical support. The IPCC Data Archive at Lawrence Livermore National Laboratory is supported by the Office of Science, U.S. Department of Energy. J. L. Lin was supported by the NASA MAP Program and NSF grant ATM-0745872. T. Shinoda was supported by NSF grant OCE-0453046 and NOAA CPO/CVP program.

REFERENCES

Blade, I., and D. L. Hartmann, 1993: Tropical intraseasonal oscillations in a simple nonlinear model. *J. Atmos. Sci.*, **50**, 2922-2939.

Bony, S., and Kerry A. Emanuel, 2005: On the Role of Moist Processes in Tropical Intraseasonal Variability: Cloud–Radiation and Moisture–Convection Feedbacks. *J. Atmos. Sci.*, **62**, 2770-2789.

Bougeault, P., 1985: A Simple Parameterization of the Large-Scale Effects of Cumulus Convection. *Monthly Weather Review*, 113, 2108–2121.

Carr, M. T., Bretherton, C. S. 2001: Convective Momentum Transport over the Tropical Pacific: Budget Estimates. J. Atmos. Sci., **58**, 1673-1693.

Del Genio, A. D., and M.-S. Yao, 1993: Efficient cumulus parameterization for long-term climate studies: The GISS scheme. *The Representation of Cumulus Convection in Numerical Models, Meteor. Monogr.,* No. 46, Amer. Meteor. Soc., 181–184.

DOBLAS-REYES, F. J., M. DÉQUÉ, F. VALERO, D. B. STEPHENSON, 1998: North Atlantic wintertime intraseasonal variability and its sensitivity to GCM horizontal resolution. Tellus A 50 (5), 573–595.

Dole, R. M., and Robert X. Black, 1990: Life Cycles of Persistent Anomalies. Part II: The Development of Persistent Negative Height Anomalies over the North Pacific Ocean. *Monthly Weather Review*, 118, 824–846.

Duchan, C.E., 1979: Lanczos filtering in one and two dimensions. *J. Appl. Meteor.*, **18**, 1016-1022.

Emanuel K. A., 1987: An air–sea interaction model of intraseasonal oscillation in the Tropics. *J. Atmos. Sci*, **44**, 2324–2340.

Emanuel, K. A., 1991: A Scheme for Representing Cumulus Convection in Large-Scale Models. *J. Atmos. Sci.*, 48, 2313–2329.

Emori, S., T. Nozawa, A. Numaguti and I. Uno (2001): Importance of cumulus parameterization for precipitation simulation over East Asia in June, J. Meteorol. Soc. Japan, 79, 939-947.

Gilman, D.L., F.J. Fuglister, and J.M. Mitchell Jr., 1963: On the Power Spectrum of "Red Noise". J. Atmos. Sci., 20, 182-184.

Gruber, A., and V. Levizzani, 2008: Assessment of global precipitation. A Project of the Global Energy and Water Cycle Experiment (GEWEX) Radiation Panel. World Climate Research Programme (WCRP) Report. 57pp.

Hayashi, Y., and D. G. Golder, 1997: United Mechanisms for the Generation of Low- and High-Frequency Tropical Waves. Part I: Control Experiments with Moist Convective Adjustment. *J. Atmos. Sci.*, **54**, 1262-1276.

Held, I. M., Steven W. Lyons, and Sumant Nigam, 1989: Transients and the Extratropical Response to El Niño. *J. Atmos. Sci.*, 46, 163-174.

Hoskins, B. J., and David J. Karoly, 1981: The Steady Linear Response of a Spherical Atmosphere to Thermal and Orographic Forcing. *J. Atmos. Sci.*, 38, 1179-1196.

Hsu H.-H., C.-H. Weng, and C.-H. Wu, 2004: Contrasting Characteristics between the Northward and Eastward Propagation of the Intraseasonal Oscillation during the Boreal Summer. *J. Climate*, 17, 727-743.

Huffman, G.J., R.F. Adler, M.M. Morrissey, S. Curtis, R. Joyce, B. McGavock, and J. Susskind, 2001: Global precipitation at one-degree daily resolution from multi-satellite observations. *J. Hydrometeor.*, **2**, 36-50.

Inness, P.M., J.M. Slingo, S.J. Woolnough, R.B. Neale and V.D. Pope, 2001: Organization of tropical convection in a GCM with varying vertical resolution: Implications for the simulation of the Madden-Julian Oscillation. Climate Dynamics, 17, 777-793.

Jenkins, G. M., and D. G. Watts, 1968: *Spectral Analysis and its Application.* Holden-Day, 525 pp.

Jiang, X., T. Li, and B. Wang, 2004: Structures and Mechanisms of the Northward Propagating Boreal Summer Intraseasonal Oscillation. J. Climate, 17, 1022-1039.

Kiladis, G. N., and K. M. Weickmann, 1997: Horizontal Structure and Seasonality of Large-Scale Circulations Associated with Submonthly Tropical Convection. Mon. Wea. Rev., 125, 1997-2013.

Kiladis, G. N., K. H. Straub, and P. T. Haertel, 2005: Zonal and vertical structure of the Madden-Julian Oscillation. *J. Atmos. Sci.*, **62**, 2790-2809.

Knutson, T. R., and K. M. Weickmann, 1987: 30–60 Day Atmospheric Oscillations: Composite Life Cycles of Convection and Circulation Anomalies. *Monthly Weather Review*, 115, 1407–1436.

Lau, N.-C., 1988: Variability of the Observed Midlatitude Storm Tracks in Relation to Low-Frequency Changes in the Circulation Pattern. *J. Atmos. Sci.*, **45**, 2718-2743.

Lau, K. M., and L. Peng, 1987: Origin of low-frequency (intraseasonal) oscillations in the tropical atmosphere. *J. Atmos. Sci.*, **44**, 950-972.

Lau, K.M., and Thomas J. Phillips, 1986: Coherent Fluctuations of Fxtratropical Geopotential Height and Tropical Convection in Intraseasonal Time Scales. *J. Atmos. Sci.*, 43, 1164-1181.

Lee, M.-I., I.-S. Kang, and B.E. Mapes, 2003: Impacts of cumulus convection parameterization on aqua-planet AGCM simulations of tropical intraseasonal variability. *J. Meteor. Soc. Japan,* **81**, 963-992.

Lin, J. L., 2007: The double-ITCZ problem in IPCC AR4 coupled GCMs: Ocean-atmosphere feedback analysis. *J. Climate*, **20**, 4497-4525.

Lin, J. L., and B. E. Mapes, 2004: Radiation budget of the tropical intraseasonal oscillation. *J. Atmos. Sci.*, **61**, 2050-2062.

Lin, J. L., B. E. Mapes, M. H. Zhang and M. Newman, 2004: Stratiform precipitation, vertical heating profiles, and the Madden-Julian Oscillation. *J. Atmos. Sci.*, **61**, 296-309.

Lin, J. L., M. H. Zhang, and B. E. Mapes, 2005: Zonal momentum budget of the Madden-Julian Oscillation: The sources and strength of equivalent linear damping. *J. Atmos. Sci*., **62**, 2172-2188.

Lin, J.L., G.N. Kiladis, B.E. Mapes, K.M. Weickmann, K.R. Sperber, W.Y. Lin, M. Wheeler, S.D. Schubert, A. Del Genio, L.J. Donner, S. Emori, J.-F. Gueremy, F. Hourdin, P.J. Rasch, E. Roeckner, and J.F. Scinocca, 2006: Tropical intraseasonal variability in 14 IPCC AR4 climate models. Part I: Convective signals. *J. Climate*, **19**, 2665-2690.

Lin, J. L., B. E. Mapes, and W. Han, 2008: What are the sources of mechanical damping in Matsuno-Gill type models? *J. Climate*, **21**, 165-179.

Lin, J. L., M.-I. Lee, D. Kim, and I.-S. Kang, 2007: Impacts of convective parameterization and moisture convective trigger on AGCM-simulated convectively coupled equatorial waves. *J. Climate*, 21, 883-909.

Madden, R. A., and P. R. Julian, 1994: Observations of the 40-50-day tropical oscillation-A review. *Mon. Wea. Rev.*, **122**, 814-837.

Mak, M., 1995: Orthogonal Wavelet Analysis: Interannual Variability in the Sea Surface Temperature. *Bulletin of the American Meteorological Society*: Vol. 76, No. 11, pp. 2179–2186.

Marcus, S. L., M. Ghil, and J. O. Dickey, 1994: The Extratropical 40-Day Oscillation in the UCLA General Circulation Model. Part I: Atmospheric Angular Momentum. J. Atmos. Sci., 51, 1431-1446.

Marcus, S. L., M. Ghil, and J. O. Dickey, 1994: The Extratropical 40-Day Oscillation in the UCLA General Circulation Model. Part II: Spatial structure. J. Atmos. Sci., 53, 1993-2004.

Mo, K. C., 1999: Alternating Wet and Dry Episodes over California and Intraseasonal Oscillations*., Mon. Wea. Rev*., **127***,* 2759–2776.

Mo, K. C., and R. W. Higgins, 1998a: Tropical influences on California precipitation. *J. Climate,* **11,** 412–430.

Mo, K. C., and R. W. Higgins, 1998b: Tropical convection and precipitation regimes in the western United States. *J. Climate,* **11,** 2404–2423.

Moorthi, S., and Suarez M. J., 1992: Relaxed Arakawa–Schubert: A parameterization of moist convection for general circulation models. *Mon. Wea. Rev.,* **120**, 978–1002.

Murakami, M., 1979: Large-Scale Aspects of Deep Convective Activity over the GATE Area. *Mon. Wea. Rev.,* 107, 994–1013.

Neelin, J. D. and N. Zeng, 2000: A quasi-equilibrium tropical circulation model - formulation. *J. Atmos. Sci.*, **57**, 1741-1766.

Nordeng, T.E., 1994: Extended versions of the convective parameterization scheme at ECMWF and their impact on the mean and transient activity of the model in the tropics. Technical Memorandum No. 206, European Centre for Medium-Range Weather Forecasts, Reading, United Kingdom.

Oort, A. H., and J. J. Yienger, 1996: Observed long-term variability in the Hadley circulation and its connection to ENSO. *J. Climate*, **9**, 2751-2767.

Pan, D.-M., and D. A. Randall (1998), A cumulus parameterization with a prognostic closure, *Q. J. R. Meteorol. Soc*., 124, 949-981.

Randall, D.A., R.A. Wood, S. Bony, R. Colman, T. Fichefet, J. Fyfe, V. Kattsov, A. Pitman, J. Shukla, J. Srinivasan, R.J. Stouffer, A. Sumi and K.E. Taylor, 2007: Cilmate Models and Their Evaluation. In: Climate Change 2007: The Physical Science Basis. Contribution of Working Group I to the Fourth Assessment Report of the Intergovernmental Panel on Climate Change [Solomon, S., D. Qin, M. Manning, Z. Chen, M. Marquis, K.B. Averyt, M.Tignor and H.L. Miller (eds.)]. Cambridge University Press, Cambridge, United Kingdom and New York, NY, USA.

Raymond, D. J., 2001: A New Model of the Madden-Julian Oscillation. *J. Atmos. Sci.*, **58**, 2807-2819.

Russell GL, Miller JR, Rind D, 1995. A coupled atmosphere-ocean model for transient climate change studies. Atmosphere-Ocean 33 (4), 683-730.

Salby M. L., R. B. Garcia, and H. H. Hendon, 1994: Planetary-scale circulations in the presence of climatological and wave-induced heating. *J. Atmos. Sci.*, **51**, 2344–2367.

Schubert, S. D., 1986: The Structure, Energetics and Evolution of the Dominant Frequency-Dependent Three-Dimensional Atmospheric Modes. *J. Atmos. Sci.*, 43, 1210–1237.

Schubert, S. D., and Chung-Kyu Park, 1991: Low-Frequency Intraseasonal Tropical-Extratropical Interactions. *J. Atmos. Sci.*, 48, 629–650.

Schubert, S. D., Max Suarez, Chung-Kyu Park, and Shrinivas Moorthi, 1993: GCM Simulations of Intraseasonal Variability in the Pacific/North American Region. *J. Atmos. Sci.*, 50, 1991–2007.

Simmons, A. J., J.M. Wallace, and G.W. Branstator, 1983: Barotropic Wave Propagation and Instability, and Atmospheric Teleconnection Patterns. *J. Atmos. Sci.*, 40, 1363–1392.

Slingo, J. M., and Coauthors, 1996: Intraseasonal oscillations in 15 atmospheric general circulation models: Results from an AMIP diagnostic subproject. *Climate Dyn.*, **12**, 325-357.

Srinivasan J., S. Gadgil, and P. J. Webster, 1993: Meridional propagation of large-scale monsoon convective zones. *Meteor. Atmos. Phys.*, **52**, 15–35.

Tiedke, M., 1989: A comprehensive mass flux scheme for cumulus parameterization in large-scale models. *Mon. Wea. Rev.,* **117**, 1779-1800.

Tokioka, T., K. Yamazaki, A. Kitoh, and T. Ose, 1988: The equatorial 30-60-day oscillation and the Arakawa-Schubert penetrative cumulus parameterization. *J. Meteor. Soc. Japan*, **66**, 883-901.

Torrence, C., and G. P. Compo. 1998: A Practical Guide to Wavelet Analysis. *Bulletin of the American Meteorological Society*: Vol. 79, No. 1, pp. 61–78.

Webster P. J., 1983: Mechanisms of monsoon low-frequency variability: Surface hydrological effects. *J. Atmos. Sci.*, **40**, 2110–2124.

Wheeler, M., and G.N. Kiladis, 1999: Convectively Coupled Equatorial Waves: Analysis of Clouds and Temperature in the Wavenumber-Frequency Domain. *J. Atmos. Sci.,* **56**, 374-399.

Zhang, G. J. and N. A. McFarlane, 1995: Sensitivity of climate simulations to the parameterization of cumulus convection in the CCC-GCM. *Atmos.-Ocean*, **3**, 407-446.

FIGURE CAPTIONS

Figure 1. Schematic depiction of the suggested mechanisms for the intraseasonal variability of western U.S. winter precipitation. Contour is the northern winter (November-April) seasonal mean GPCP precipitation. The first contour is 1 mm/day and contour interval is 2 mm/day.

Figure 2. Northern winter (November-April) seasonal mean precipitation for observation and 14 IPCC AR4 models. The first contour is 2 mm/day and contour interval is 2 mm/day.

Figure 3. Meridional profile of northern winter (November-April) seasonal mean precipitation averaged between 235E-245E for observation and 14 models.

Figure 4. Horizontal distribution of the standard deviation of total intraseasonal (10-90 day) precipitation anomaly during northern summer (November-April). The first contour is 2 mm/day and the contour interval is 1 mm/day.

Figure 5. Meridional profile of the total intraseasonal (10-90 day) variance of precipitation anomaly averaged between 235E-245E.

Figure 6. Wavelet spectrum of precipitation averaged between 40-45N and 235-245E. Only spectral peaks above the 95% confidence level are plotted.

Figure 7. Same as Figure 5 but for the variance of the 40-day mode.

Figure 8. Lag-correlation of the 40-day mode precipitation anomaly averaged between 235E-245E with respect to itself at 37.5N240E. Shading denotes the regions where lag-correlation is above the 95% confidence level.

Figure 9. Lag-correlation of temperature averaged between 30N-35N, 235E-245E versus the 40-day mode precipitation anomaly at the same location for observation (NCEP

reanalysis) and seven models. Shading denotes the area where correlation is above the 95% confidence level, with dark (light) shading for positive (negative) correlation.

Figure 10. Same as Figure 9 but for geopotential height.

Figure 11. Same as Figure 9 but for divergence.

Figure 12. Linear correlation of the 40-day mode precipitation anomaly versus itself averaged between 35N-40N, 235E-245E. Shading denotes the area where correlation is above the 95% confidence level, with dark (light) shading for positive (negative) correlation.

Figure 13. Same as Figure 5 but for the variance of the 22-day mode.

Figure 14. Lag-correlation of the 22-day mode precipitation anomaly averaged between 235E-245E with respect to itself at 37.5N240E. Shading denotes the regions where lag-correlation is above the 95% confidence level.

Figure 15. Same as Figure 12 but for the 22-day mode.

Table 1 List of models that participate in this study

Modeling Groups	IPCC ID (Label in Figures)	Grid type/ Resolution/ Model top	Deep convection scheme / Modification	Downdrafts* SC/UC/Meso	Closure/ Trigger
NOAA / Geophysical Fluid Dynamics Laboratory	GFDL-CM2.0 (GFDL2.0)	Gridpoint 144*90*L24 3mb	Moorthi and Suarez (1992) / Tokioka et al. (1988)	N/N/N	CAPE/ Threshold
NOAA/ Geophysical Fluid Dynamics Laboratory	GFDL-CM2.1 (GFDL2.1)	Gridpoint 144*90*L24 3mb	Moorthi and Suarez (1992) / Tokioka et al. (1988)	N/N/N	CAPE/ Threshold
National Center for Atmospheric Research	CCSM3 (CCSM3)	Spectral T85*L26 2.2mb	Zhang and McFarlane (1995)	Y/N/N	CAPE
National Center for Atmospheric Research	PCM (PCM)	Spectral T42*L26 2.2mb	Zhang and McFarlane (1995)	Y/N/N	CAPE
NASA/ Goddard Institute for Space Studies	GISS-AOM (GISS-AOM)	Gridpoint 90*60*L12	Russell et al. (1995)	N/N/N	CAPE
NASA/ Goddard Institute for Space Studies	GISS-ER (GISS-ER)	Gridpoint 72*46*L20 0.1mb	Del Genio and Yao (1993)	Y/N/N	Cloud base buoyancy
Center for Climate System Research, National Institute for Environmental Studies, & Frontier Research Center for Global Change	MIROC3.2–hires (MIROC-hires)	Spectral T106*L56	Pan and Randall (1998) / Emori et al. (2001)	Y/N/N	CAPE/ Relative humidity
Same as above	MIROC3.2-medres (MIROC-medres)	Spectral T42*L20 30 km	Pan and Randall (1998) / Emori et al. (2001)	Y/N/N	CAPE/ Relative humidity
Meteorological Research Institute	MRI-CGCM2.3.2 (MRI)	Spectral T42*L30 0.4mb	Pan and Randall (1998)	Y/N/N	CAPE
Canadian Centre for Climate Modeling & Analysis	CGCM3.1 -T47 (CGCM)	Spectral T47*L32 1mb	Zhang & McFarlane (1995)	Y/N/N	CAPE
Max Planck Institute for Meteorology	ECHAM5/ MPI-OM (MPI)	Spectral T63*L31 10mb	Tiedtke (1989) / Nordeng (1994)	Y/N/N	CAPE/ Moisture convergence
Institute Pierre Simon Laplace	IPSL-CM4 (IPSL)	Gridpoint 96*72*L19	Emanuel (1991)	Y/Y/N	CAPE
Mateo-France / Centre National de Recherches Météorologiques	CNRM-CM3 (CNRM)	Spectral T63*L45 0.05mb	Bougeault (1985)	N/N/N	Kuo
CSIRO Atmospheric Research	CSIRO Mk3.0 (CSIRO)	Spectral T63*L18 4mb	Gregory and Rowntree (1990)	Y/N/N	Cloud base buoyancy

* For downdrafts, SC means saturated convective downdrafts, UC means unsaturated convective downdrafts, and Meso means mesoscale downdrafts.

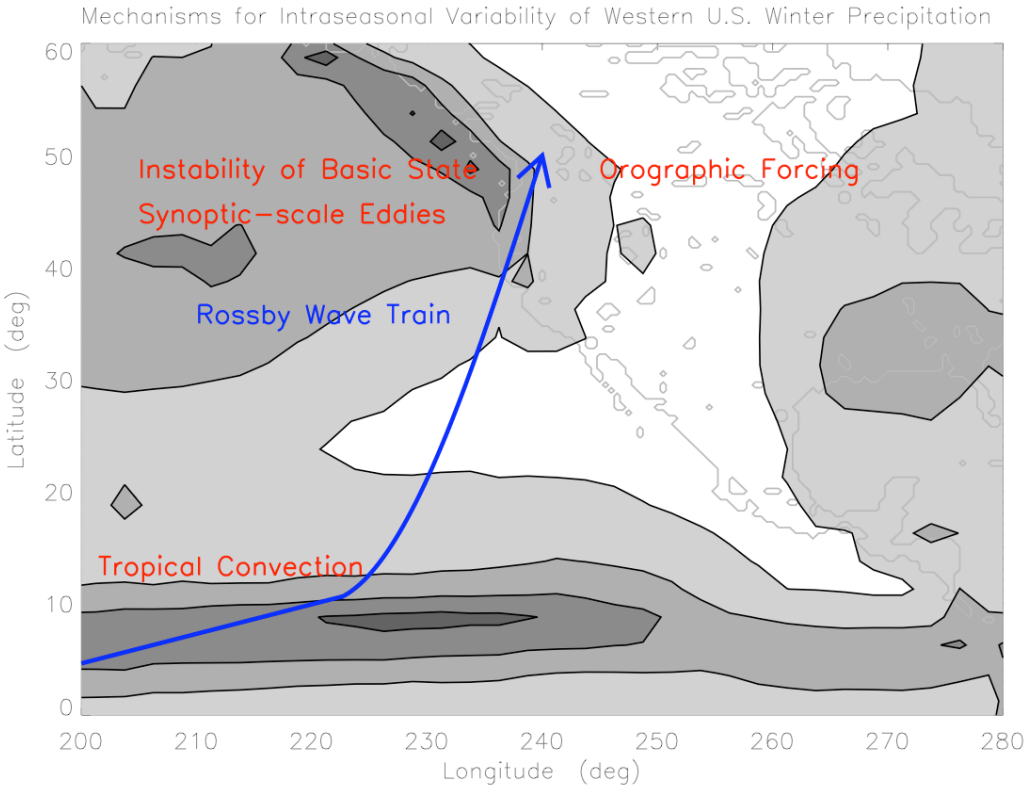

Figure 1. Schematic depiction of the suggested mechanisms for the intraseasonal variability of western U.S. winter precipitation. Contour is the northern winter (November-April) seasonal mean GPCP precipitation. The first contour is 1 mm/day and contour interval is 2 mm/day.

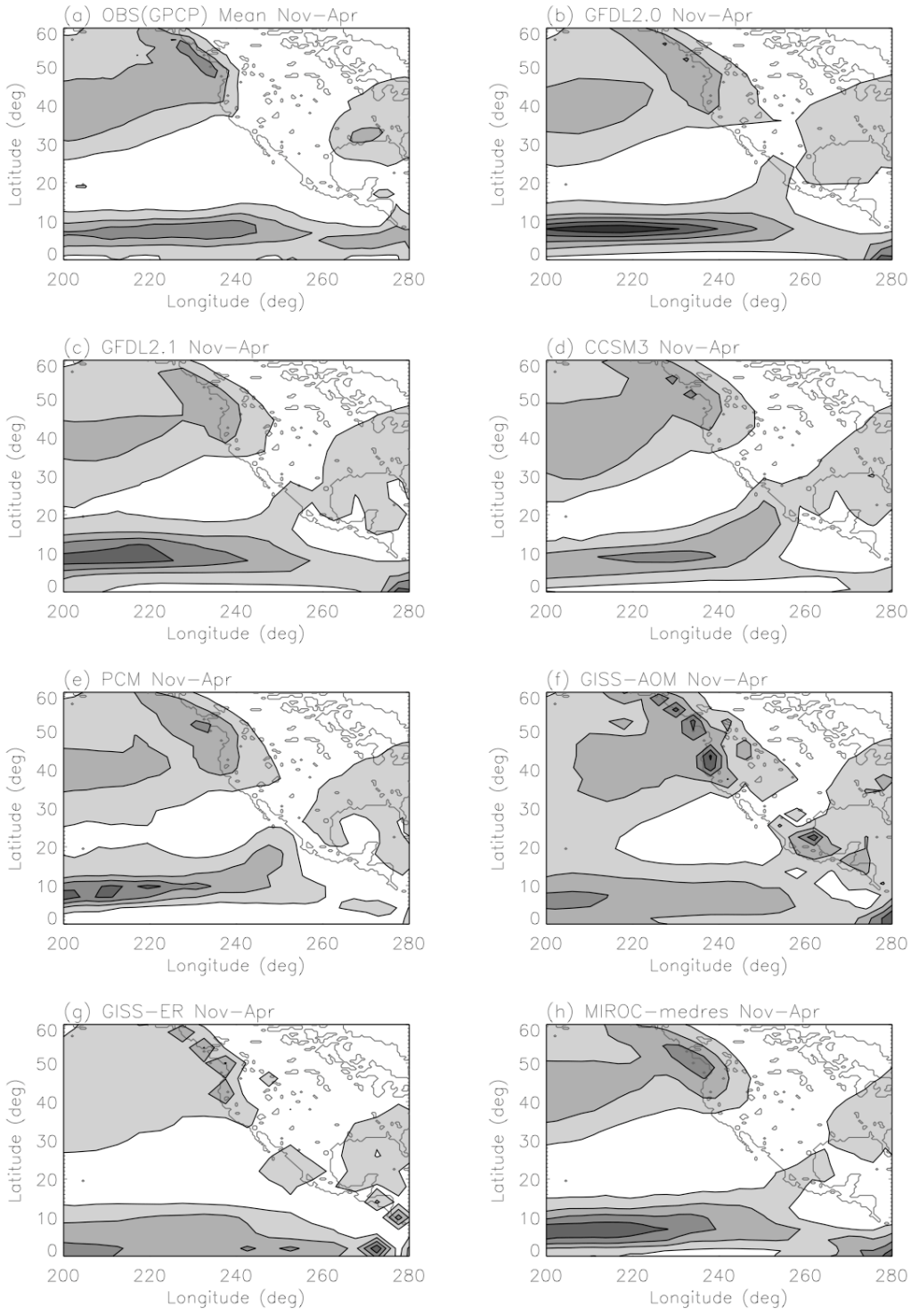

Figure 2. Northern winter (November-April) seasonal mean precipitation for observation and 14 IPCC AR4 models. The first contour is 2 mm/day and contour interval is 2 mm/day.

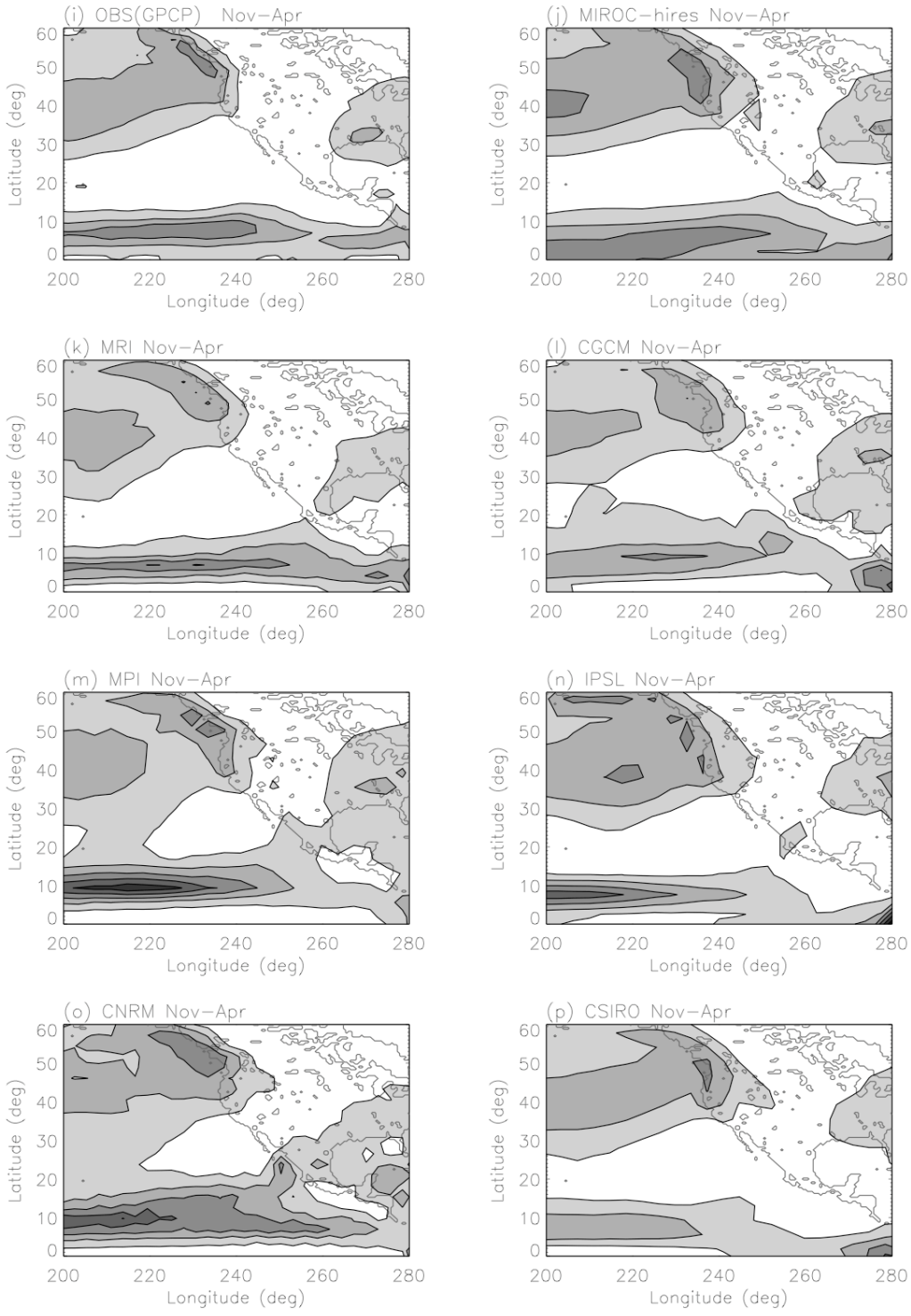

Figure 2. Continued.

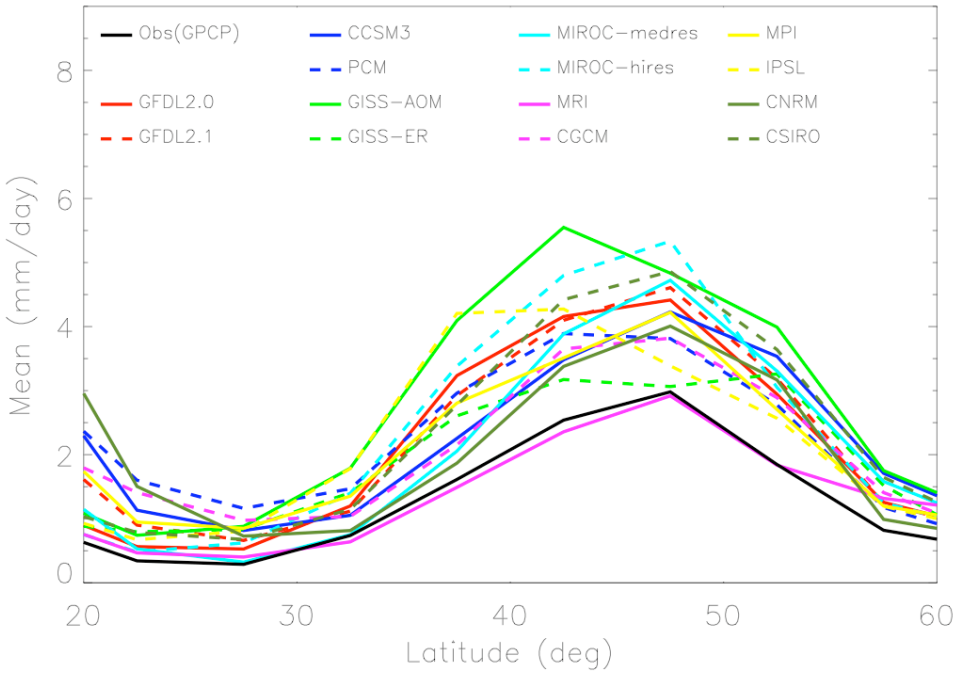

Figure 3. Meridional profile of northern winter (November-April) seasonal mean precipitation averaged between 235E-245E for observation and 14 models.

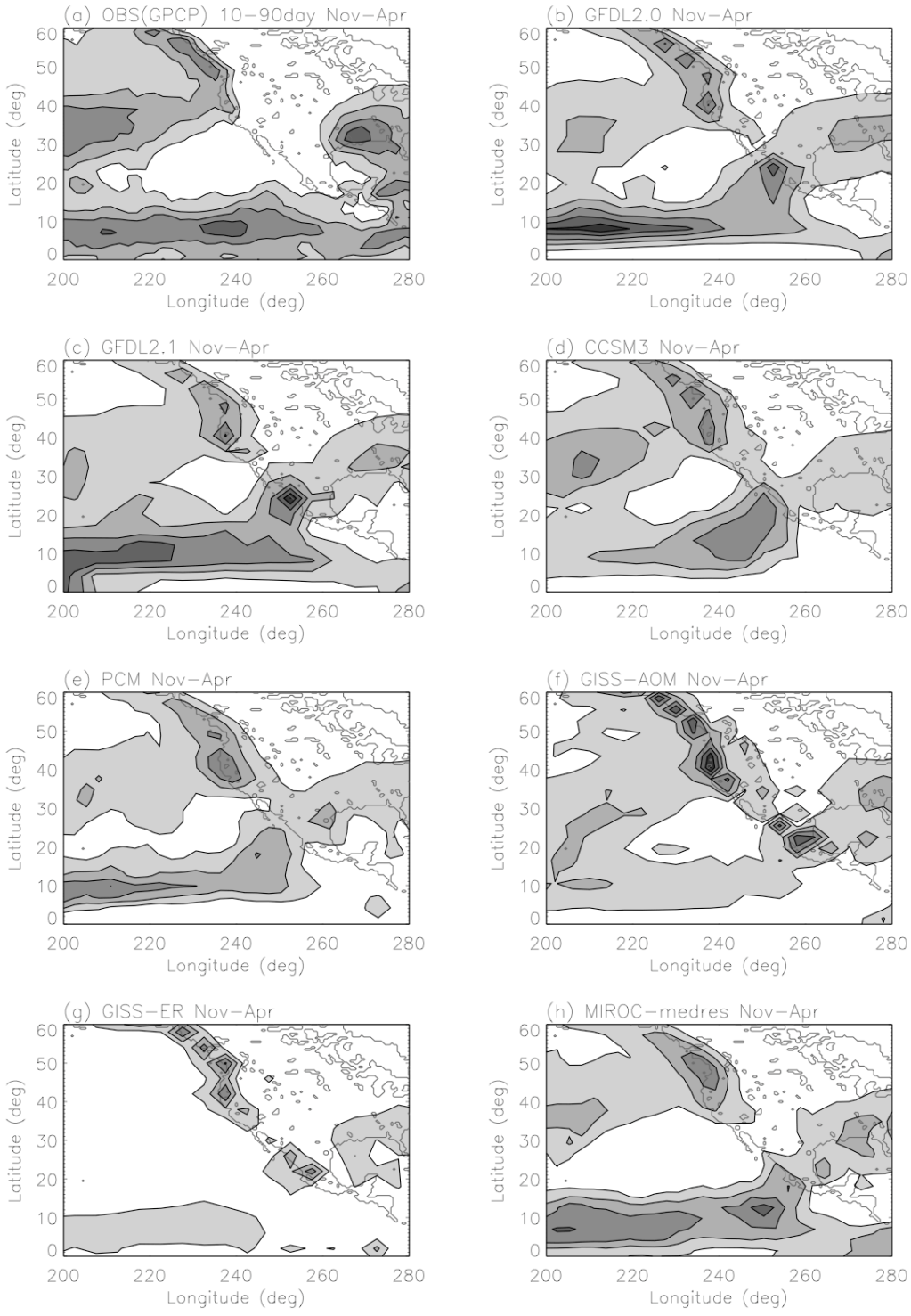

Figure 4. Horizontal distribution of the standard deviation of total intraseasonal (10-90 day) precipitation anomaly during northern summer (November-April). The first contour is 2 mm/day and the contour interval is 1 mm/day.

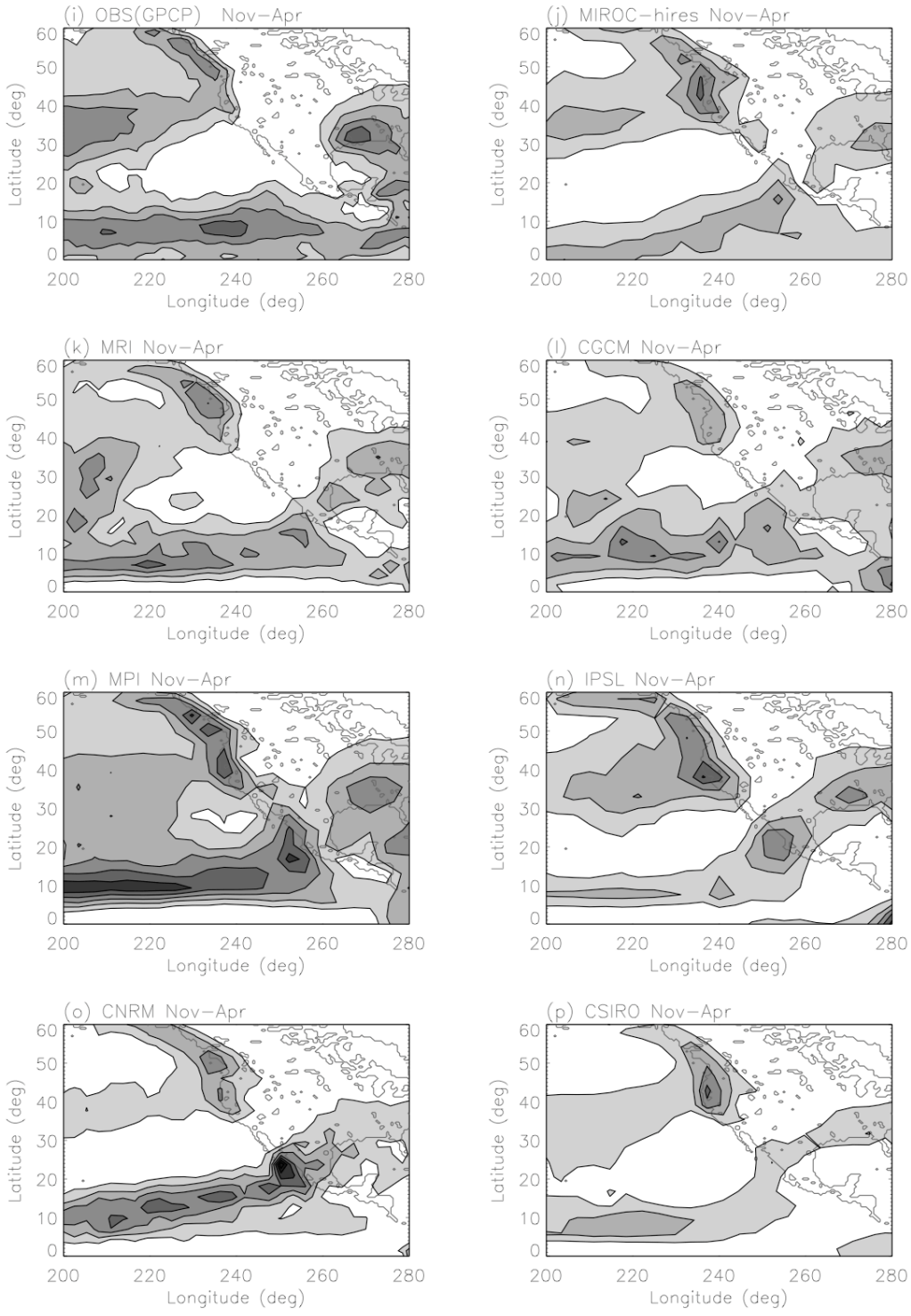

Figure 4. Continued.

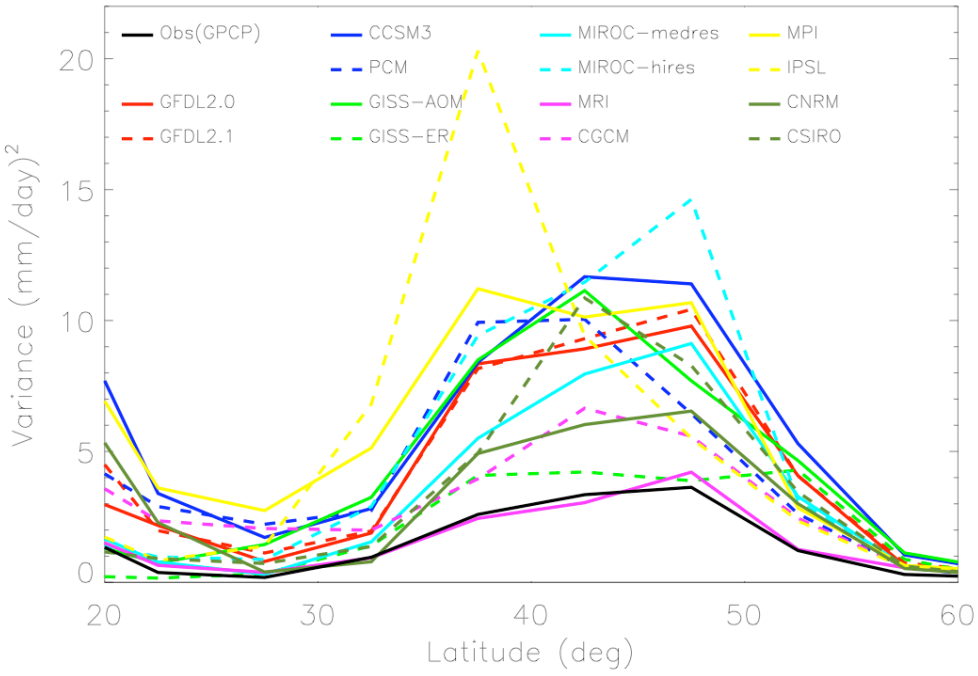

Figure 5. Meridional profile of the total intraseasonal (10-90 day) variance of precipitation anomaly averaged between 235E-245E.

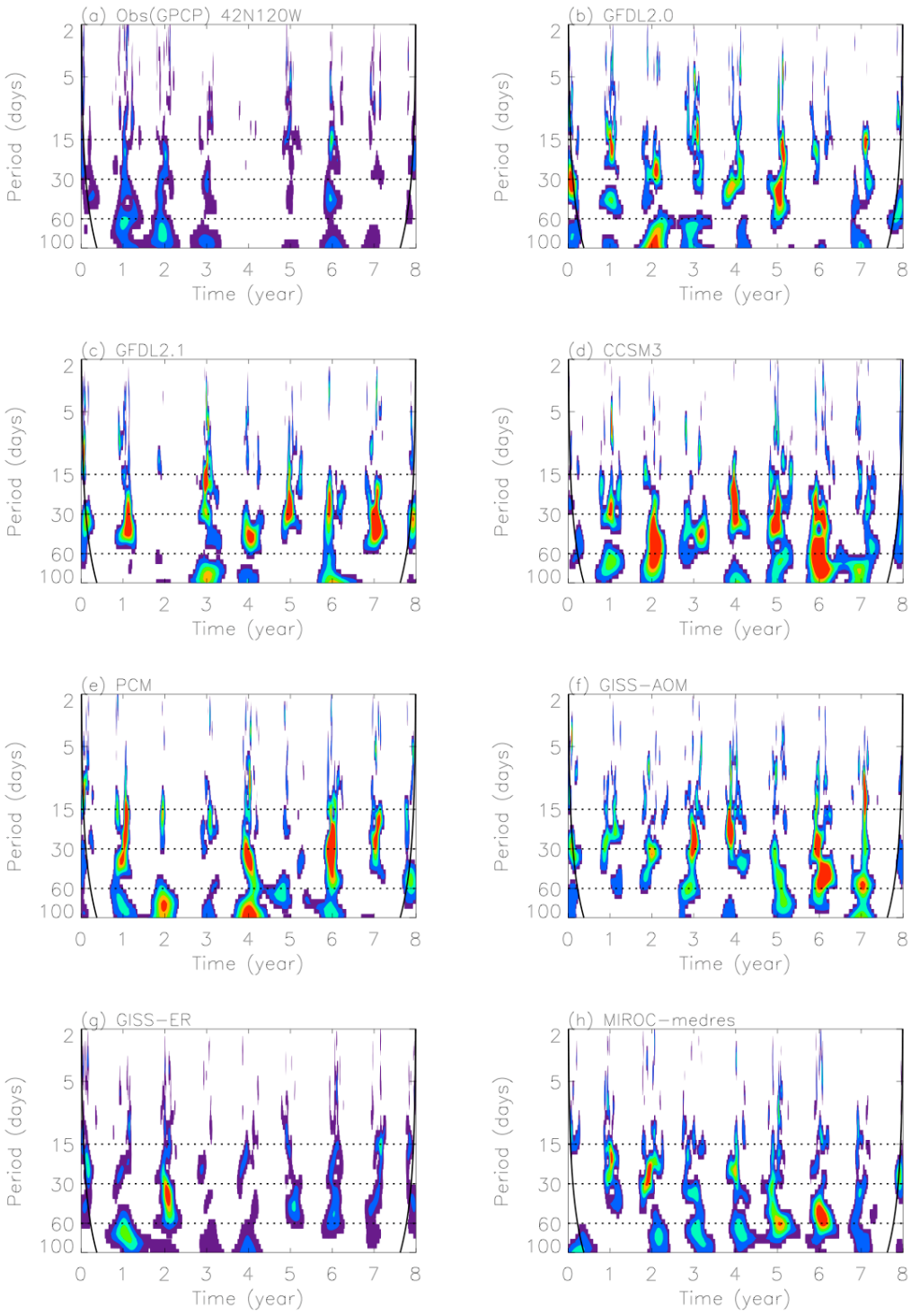

Figure 6. Wavelet spectrum of precipitation averaged between 40-45N and 235-245E. Only spectral peaks above the 95% confidence level are plotted.

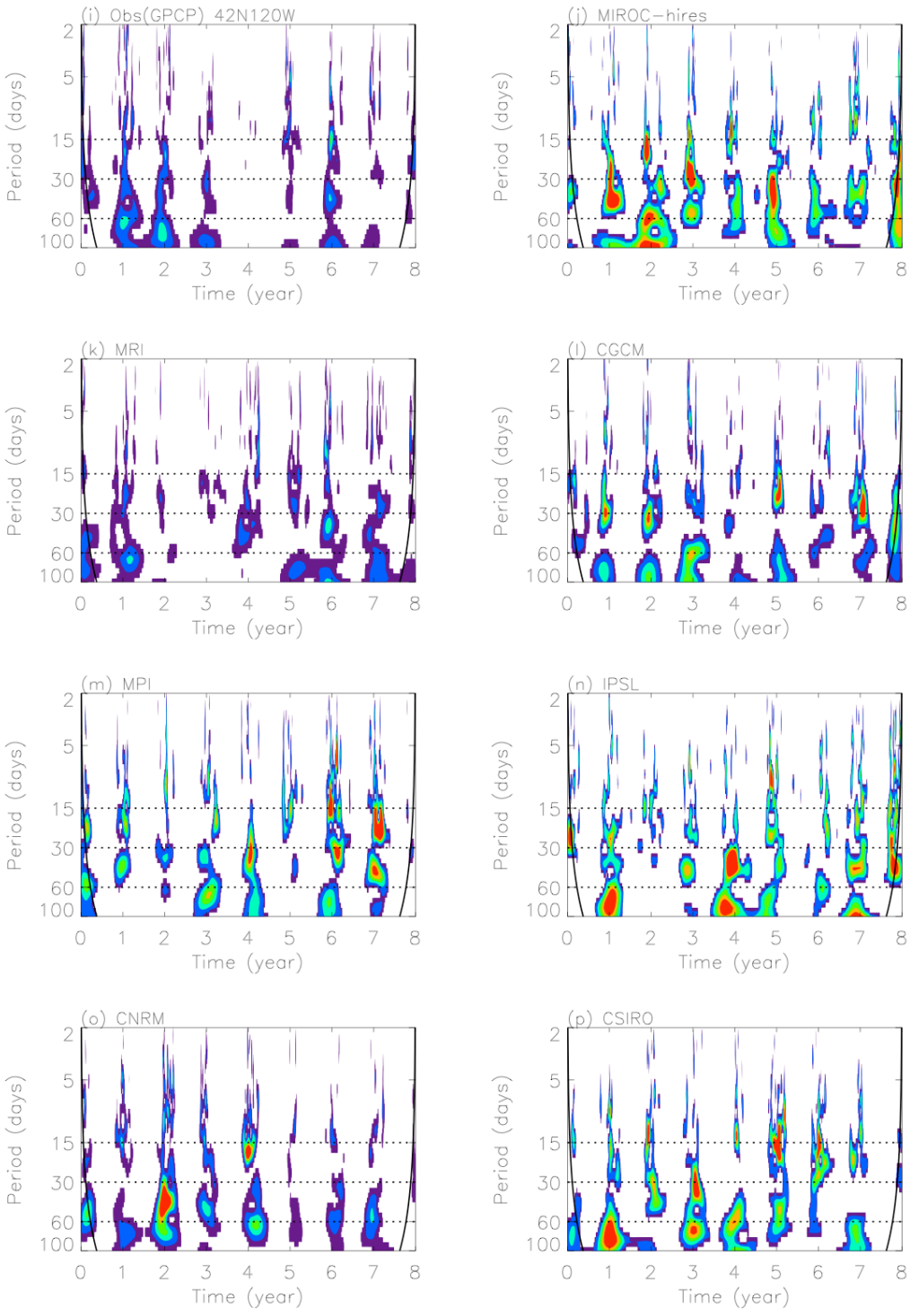

Figure 6. Continued.

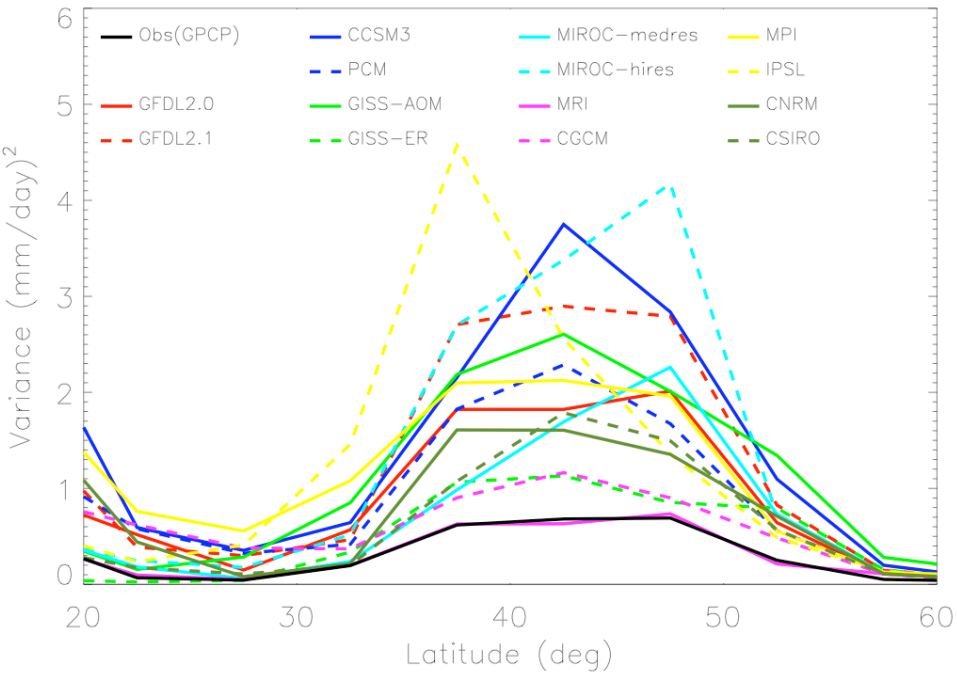

Figure 7. Same as Figure 5 but for the variance of the 40-day mode.

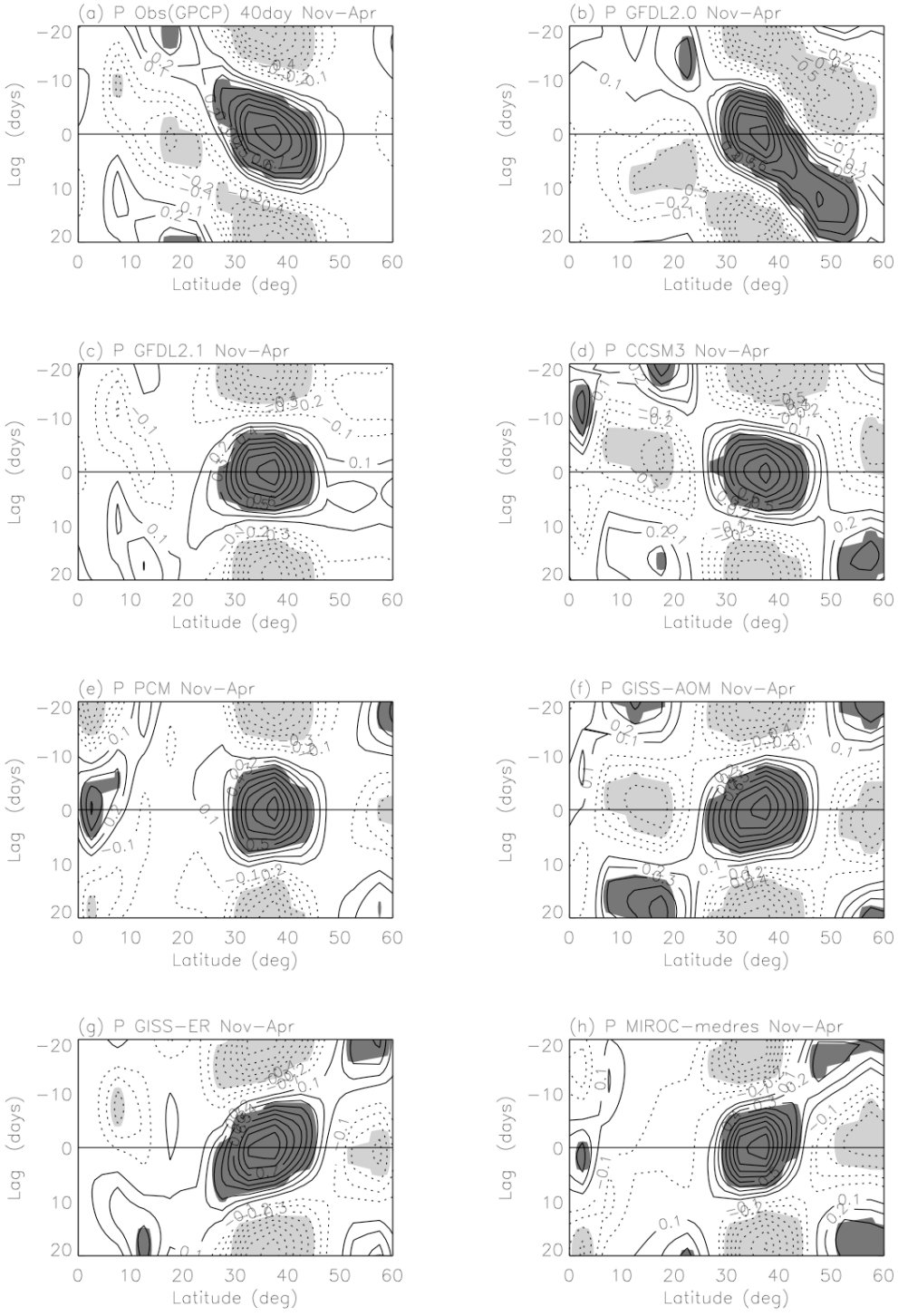

Figure 8. Lag-correlation of the 40-day mode precipitation anomaly averaged between 235E-245E with respect to itself at 37.5N240E. Shading denotes the regions where lag-correlation is above the 95% confidence level.

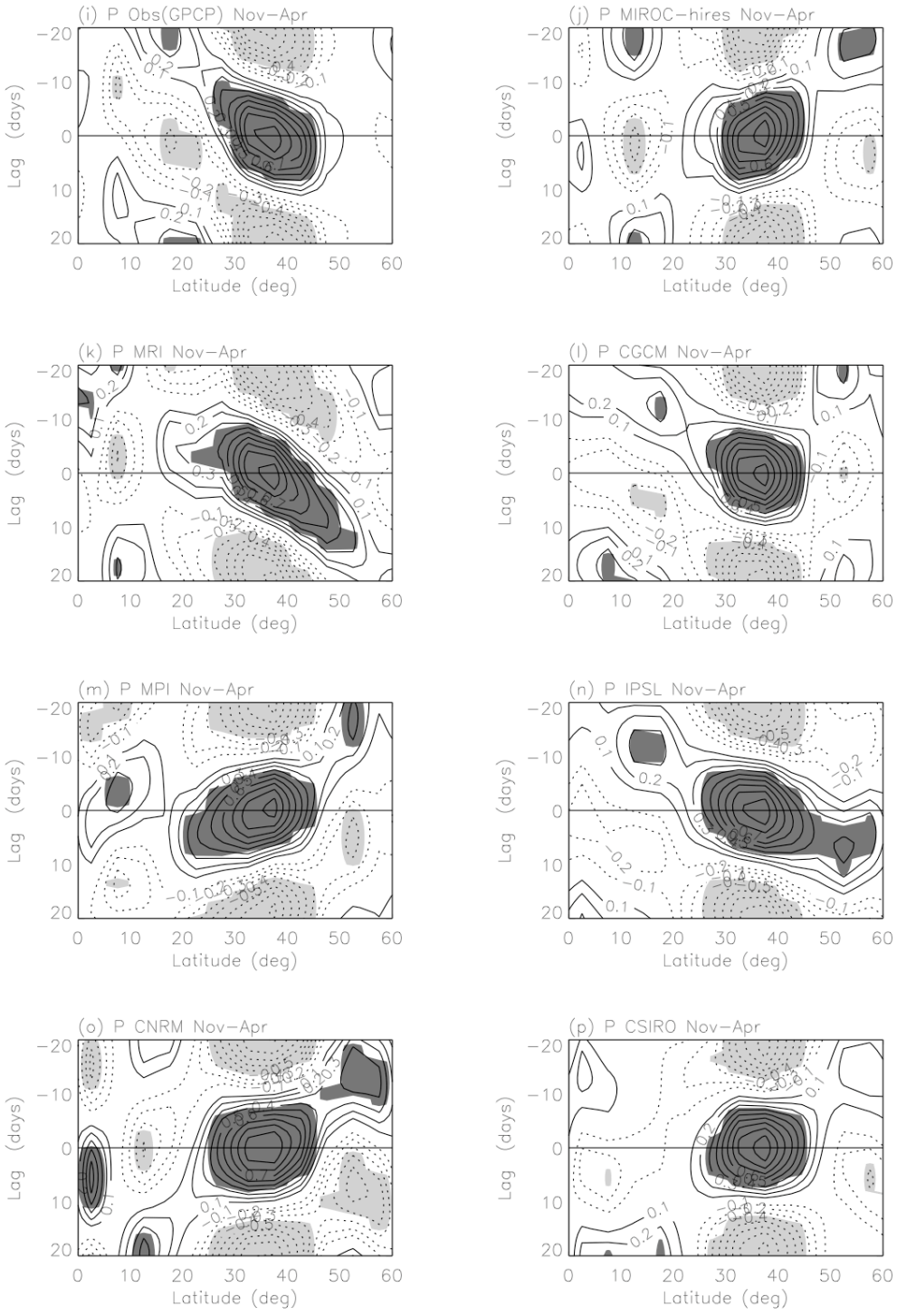

Figure 8. Continued.

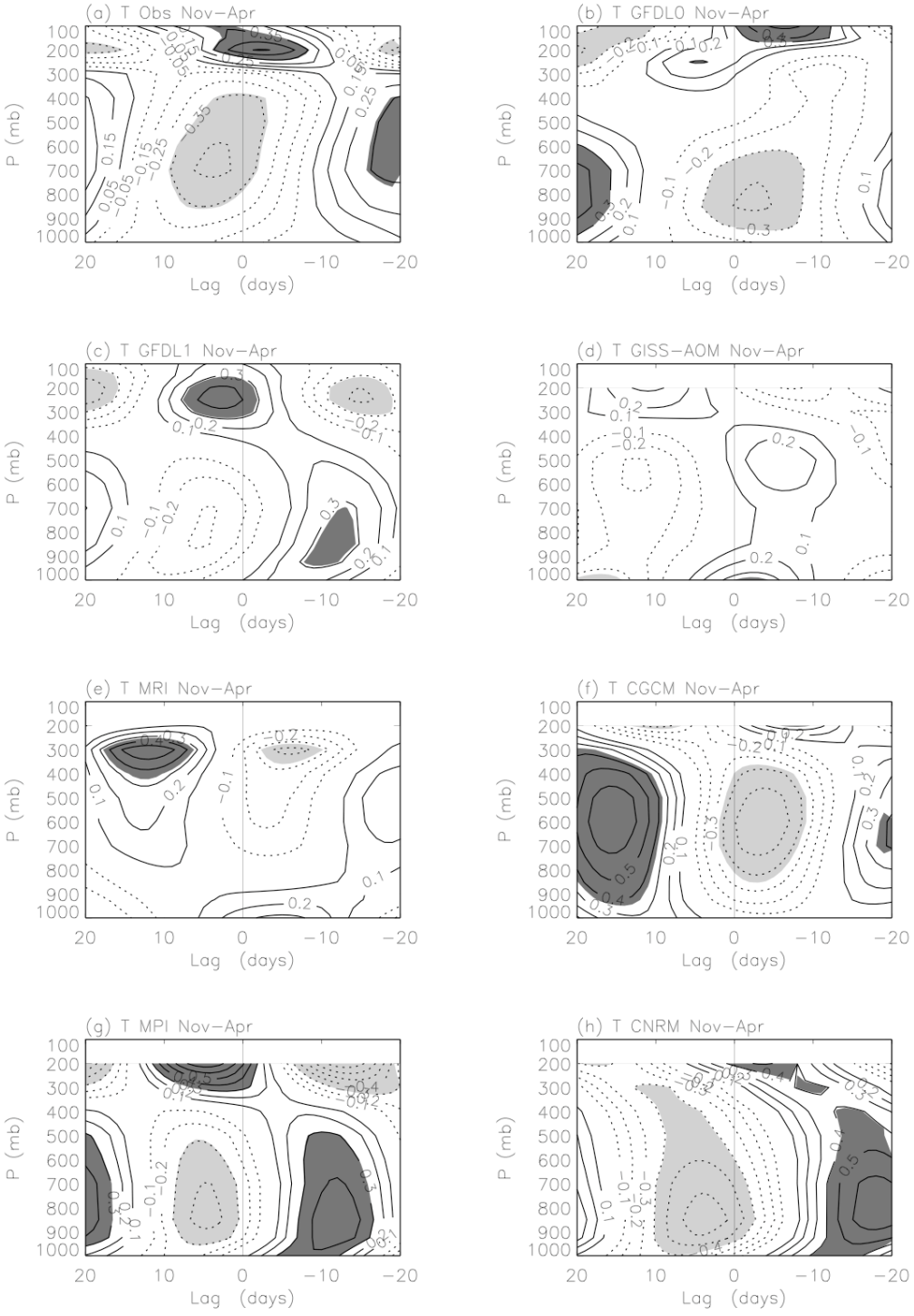

Figure 9. Lag-correlation of temperature averaged between 30N-35N, 235E-245E versus the 40-day mode precipitation anomaly at the same location for observation (NCEP reanalysis) and seven models. Shading denotes the area where correlation is above the 95% confidence level, with dark (light) shading for positive (negative) correlation.

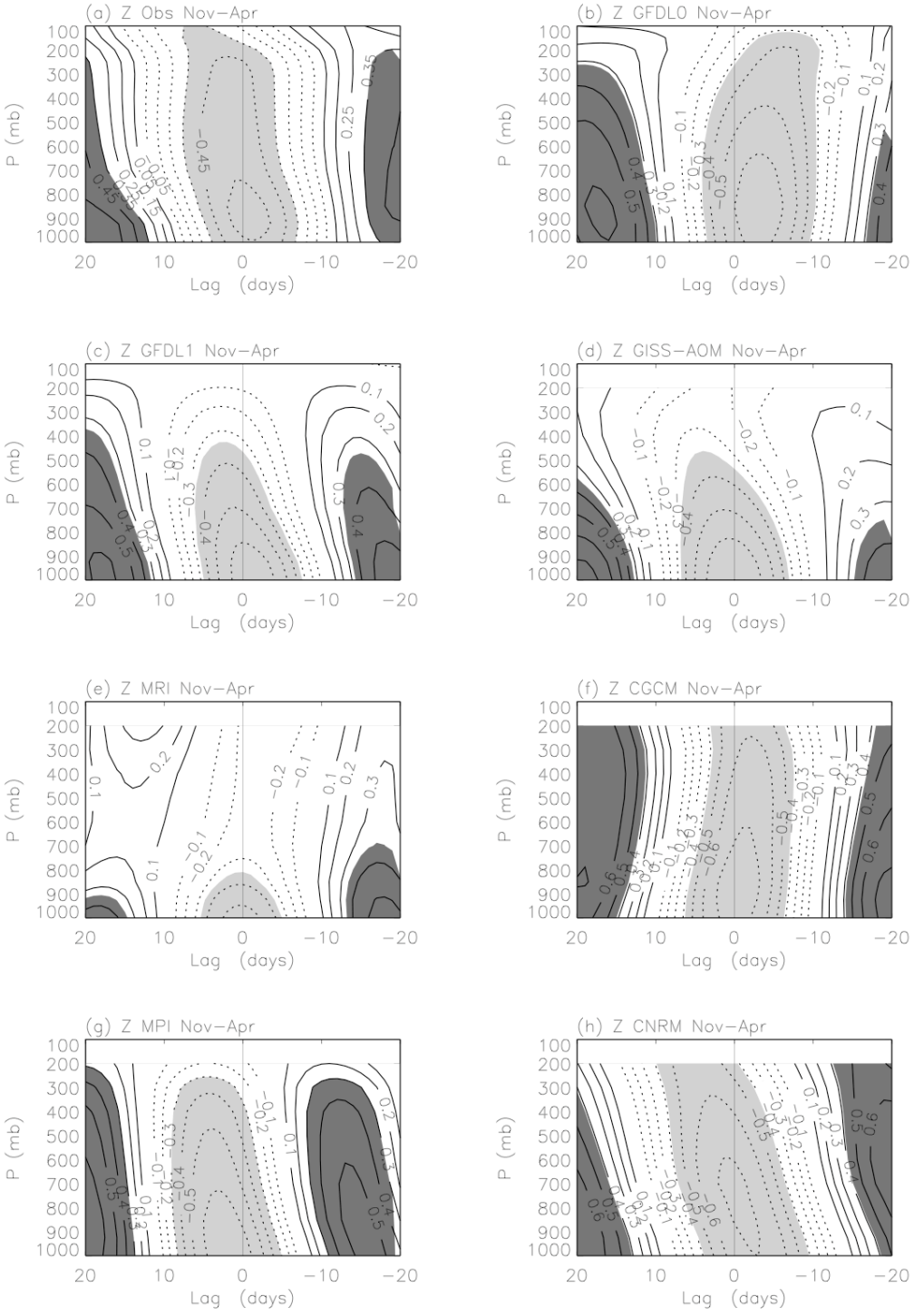

Figure 10. Same as Figure 9 but for geopotential height.

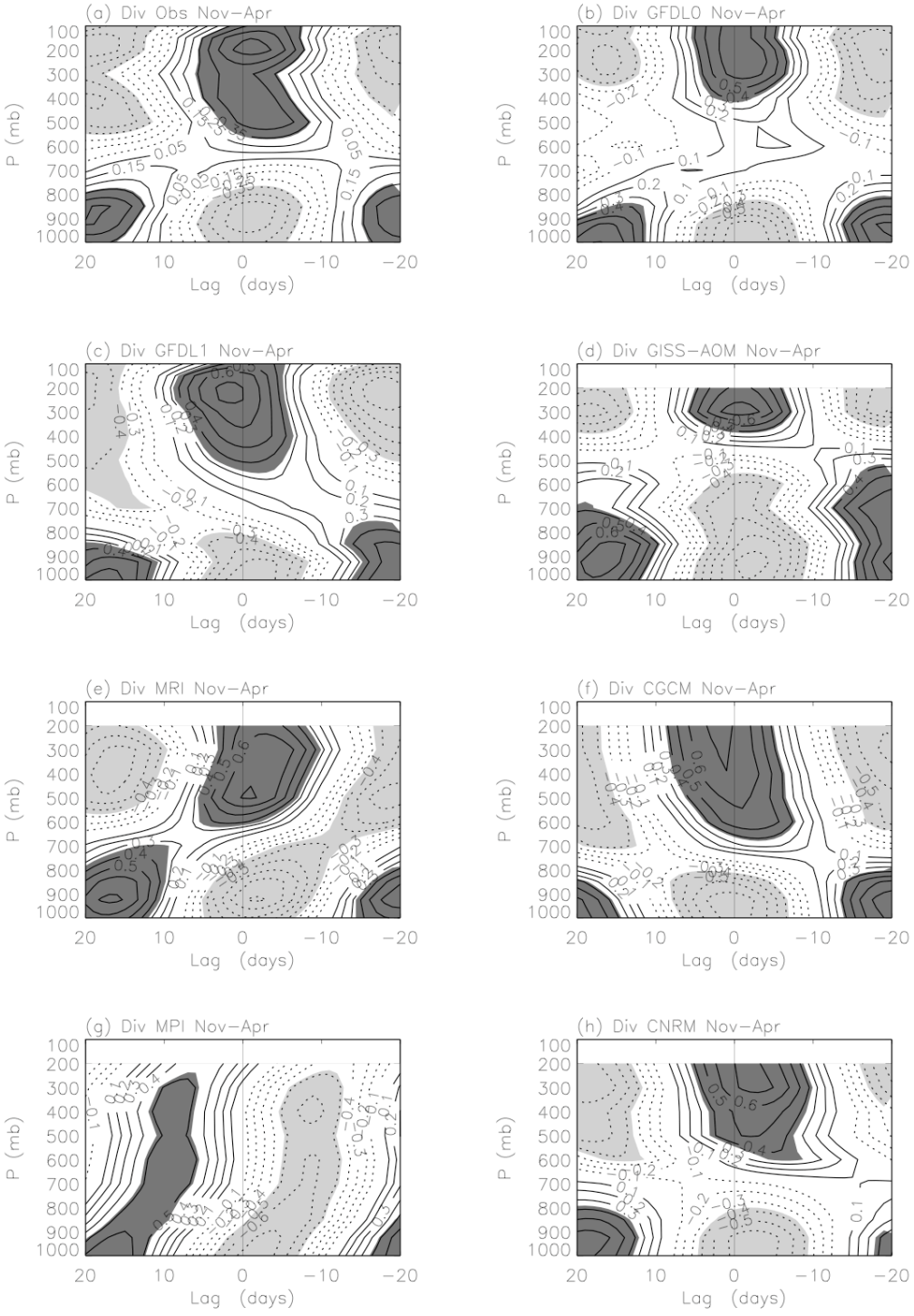

Figure 11. Same as Figure 9 but for divergence.

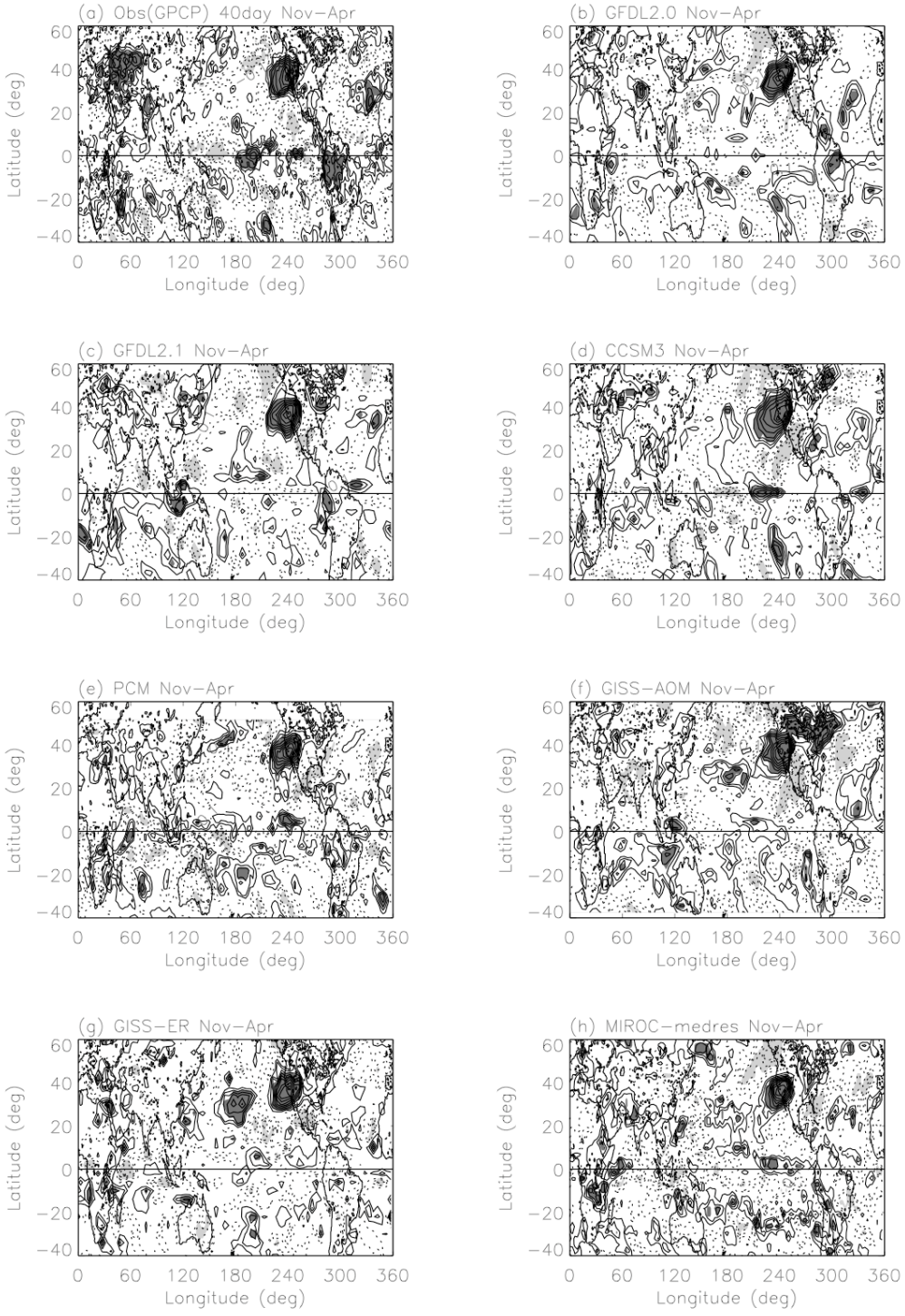

Figure 12. Linear correlation of the 40-day mode precipitation anomaly versus itself averaged between 35N-40N, 235E-245E. Shading denotes the area where correlation is above the 95% confidence level, with dark (light) shading for positive (negative) correlation.

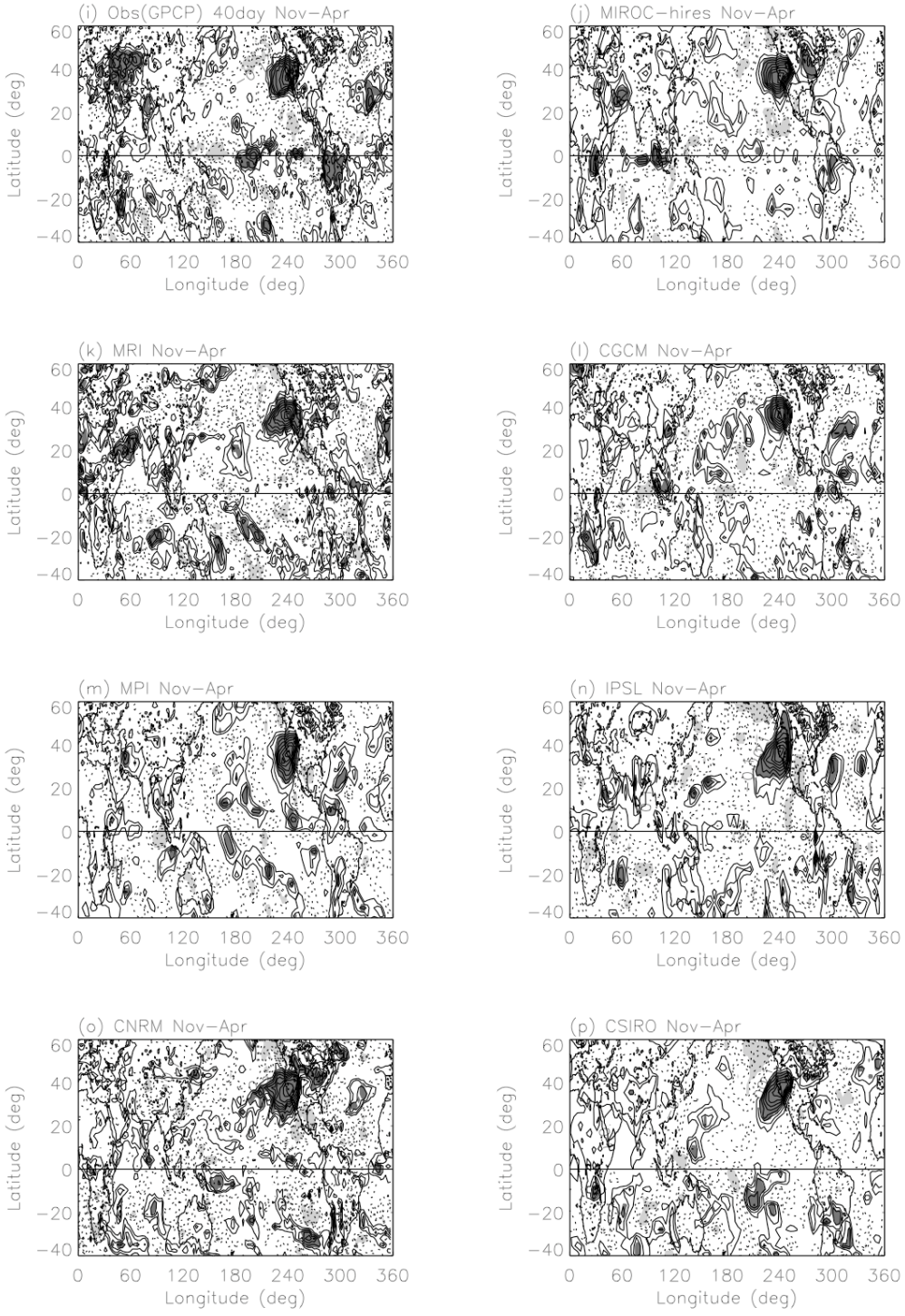

Figure 12. Continued.

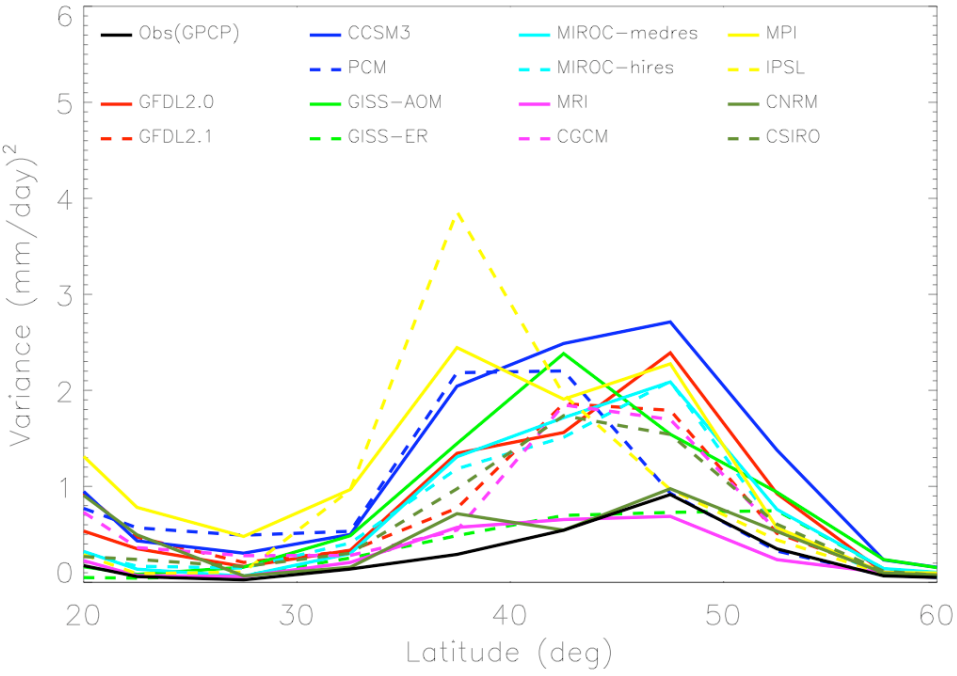

Figure 13. Same as Figure 5 but for the variance of the 22-day mode.

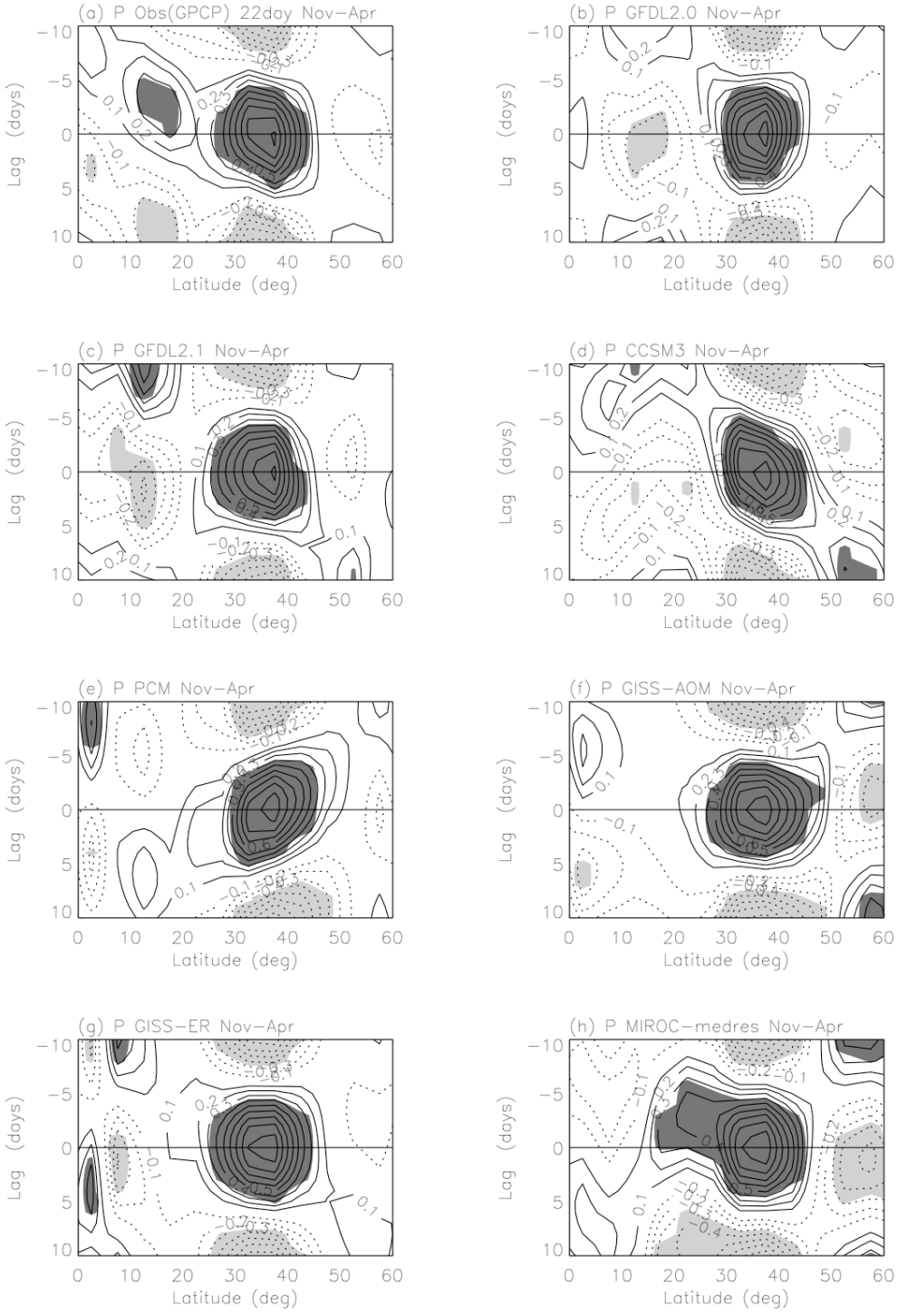

Figure 14. Lag-correlation of the 22-day mode precipitation anomaly averaged between 235E-245E with respect to itself at 37.5N240E. Shading denotes the regions where lag-correlation is above the 95% confidence level.

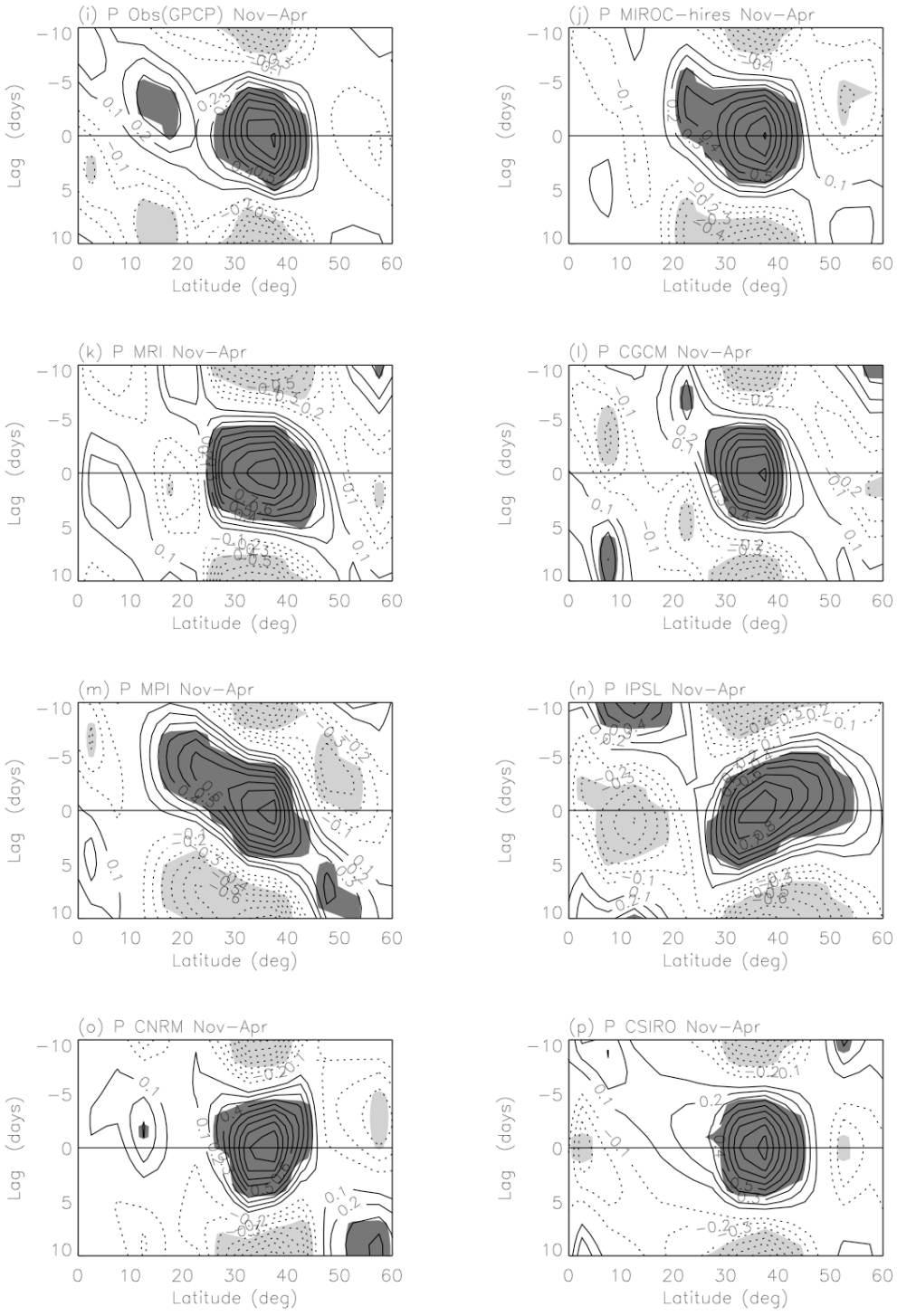

Figure 14. Continued.

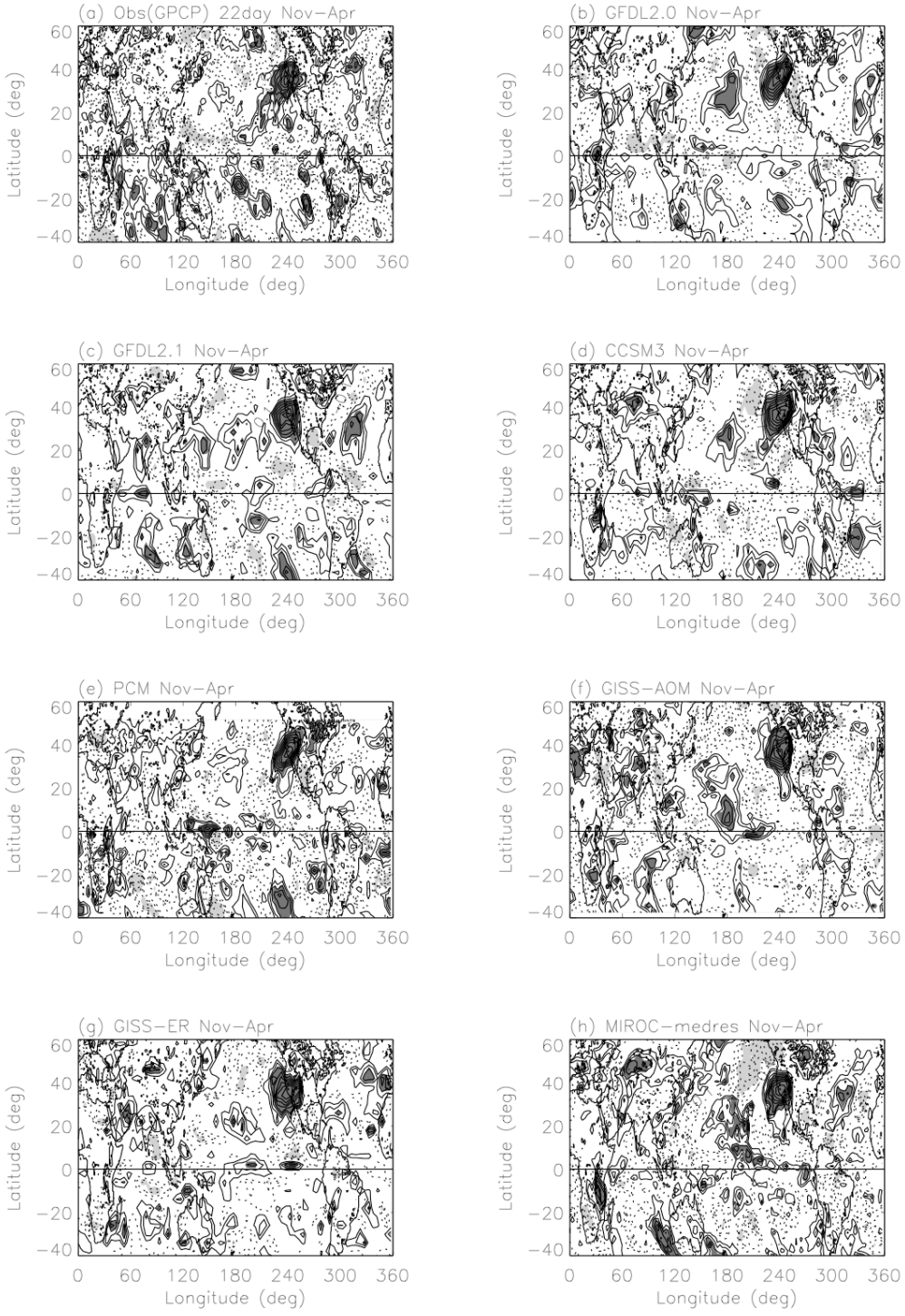

Figure 15. Same as Figure 12 but for the 22-day mode.

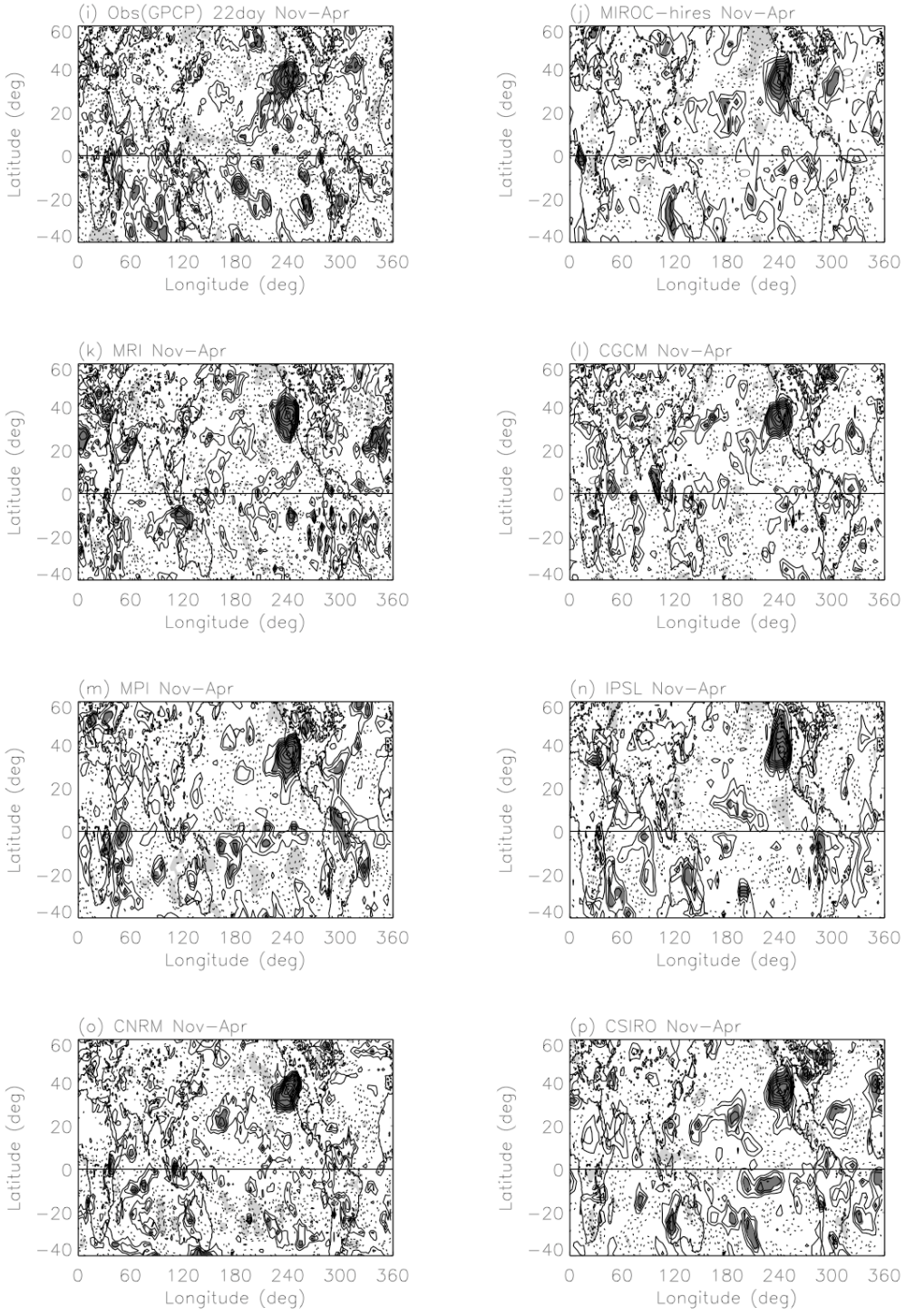

Figure 15. Continued.